CALIBRATION AND DATA REDUCTION ALGORITHMS FOR

NON-CONVENTIONAL MULTI-HOLE PRESSURE PROBES

A Thesis

by

VIJAY RAMAKRISHNAN

Submitted to the Office of Graduate Studies of
Texas A&M University
in partial fulfillment of the requirements for the degree of

MASTER OF SCIENCE

May 2004

Major Subject: Aerospace Engineering

CALIBRATION AND DATA REDUCTION ALGORITHMS FOR

NON-CONVENTIONAL MULTI-HOLE PRESSURE PROBES

A Thesis

by

VIJAY RAMAKRISHNAN

Submitted to Texas A&M University
in partial fulfillment of the requirements
for the degree of

MASTER OF SCIENCE

Approved as to style and content by:

Othon K. Rediniotis (Chair of Committee)	Paul G. Cizmas (Member)
Luis San Andres (Member)	Walter E. Haisler (Head of Department)

May 2004

Major Subject: Aerospace Engineering

ABSTRACT

Calibration and Data Reduction Algorithms for

Non-conventional Multi-hole Pressure Probes. (May 2004)

Vijay Ramakrishnan, B.Tech., Indian Institute of Technology-Madras, India

Chair of Advisory Committee: Dr. Othon K. Rediniotis

This thesis presents the development of calibration and data-reduction algorithms for non-conventional multi-hole pressure probes. The algorithms that have been developed for conventional 5- and 7-hole probes are not optimal for probes with port arrangements (on the probe tip) that are non-conventional. Conventional algorithms utilize the axisymmetry of the port distribution pattern to define the non-dimensional pressure coefficients. These coefficients are typically defined specifically for these patterns, but fail to correctly represent different patterns of port arrangements, such as patterns without axisymmetry or regularity. The algorithms introduced herein can handle any pattern of port arrangement, from axisymmetric and regular to random. Moreover, they eliminate the need to separate the measurement domain of a probe to "low-angle" and "high-angle" regimes, typical in conventional 5- and 7-hole-probe algorithms that require two different sets of pressure coefficient definitions and procedures. Additionally, the algorithms have been formulated such that they facilitate redundancy implementations, especially in applications where such redundancy is important, such as air-data systems.

The developed algorithms are first applied to a non-conventional probe, a nearly omni-directional 18-hole probe, and demonstrate very high flow measurement accuracy. Subsequently, the algorithms were applied to a new 12-hole, nearly omni-directional, flow velocity measurement probe capable of measuring reversed flows. The new 12-hole

design offers several advantages over a previously developed, 18-hole, nearly omni-directional probe. The probe is optimized in the sense that, regardless of the flow direction, it allows calculation of the 4 unknown flow quantities, i.e. the two flow angles, the velocity magnitude and the static pressure, with the minimum necessary number of holes/ports on the probe tip. This probe also has a non-conventional arrangement of its pressure ports and therefore the new calibration and data-reduction algorithms can be effectively employed. With theoretically generated pressure data for the 12-hole probe, the coefficient definitions are analyzed and found to be well-behaved.

ACKNOWLEDGEMENTS

TABLE OF CONTENTS

LIST OF TABLES

Page

LIST OF FIGURES

NOMENCLATURE

ENGLISH SYMBOLS

A_θ, B_θ	=	Polynomial coefficients for C_θ expression [-]
A_ϕ, B_ϕ	=	Polynomial coefficients for C_ϕ expression [-]
Cp	=	Pressure coefficient [-]
C_s	=	Static pressure coefficient [-]
C_t	=	Total pressure coefficient [-]
C_θ	=	Cone-angle coefficient [-]
C_ϕ	=	Roll-angle coefficient [-]
$C_{\theta\text{-CAL}}$	=	Cone-angle coefficient from calibration database [-]
$C_{\phi\text{-CAL}}$	=	Roll-angle coefficient from calibration database [-]
d	=	Euclidean distance [-]
P_i	=	Pressure at port 'i' [Pa]
P_s	=	Static pressure [Pa]
P_t	=	Total pressure [Pa]
q	=	Freestream dynamic pressure [Pa]
q_{est}	=	Estimated freestream dynamic pressure [Pa]
R, S, T	=	Polynomial coefficients for q_{est} [-]
T_s	=	Static temperature [K]
T_t	=	Total temperature [K]
u	=	Velocity magnitude [m/s]
U	=	Freestream velocity magnitude [m/s]

GREEK SYMBOLS

α	=	Pitch angle [deg]
β	=	Yaw angle [deg]
$\Delta P1$	=	Difference in port pressures: P_1-P_3 [Pa]
$\Delta P2$	=	Difference in port pressures: P_2-P_3 [Pa]
$\Delta P3$	=	Difference in port pressures, P_3-P_4 [Pa]
Θ	=	Cone angle in global coordinate system [deg]
Φ	=	Roll angle in global coordinate system [deg]
θ	=	Cone angle in local coordinate system [rad]
ϕ	=	Roll angle in local coordinate system [rad]
θ_0	=	Polynomial coefficient for θ expression [rad]
ϕ_0	=	Polynomial coefficient for ϕ expression [rad]
λ	=	Scaling factor [-]
ρ	=	Density of air [kg/m^3]
ψ	=	Central angle between any two points on a sphere [rad]

1 INTRODUCTION

Multi-hole pressure probes have, over the years, been used to resolve the three-dimensional velocity vector and static and total pressures at the point of measurement in a flowfield. Such devices include 5- and 7-hole probes (Bryer and Pankhurst [1], Everett and Gerner [2], Kjelgaard [3], Zilliac [4], Rediniotis et al. [5]) and 18-hole, nearly omni-directional probes (Kinser and Rediniotis [6]). There are of course other types of pressure probes such as pitot-static probes and yaw probes, which, however, are not of interest here, since they cannot resolve all three components of the velocity vector.

Numerous calibration and data-reduction algorithms and procedures have been developed over the years for steady measurements with typical 5- and 7-hole probes. One of the approaches relates the flow velocity magnitude and incidence angle to a theoretical model, such as a potential flow model. Based on the theoretical model, the port pressures are related to the flow incidence and velocity magnitude. Kjelgaard [3] used this technique on a hemispherical tipped 5-hole probe. However, the fact that the measurement accuracy expected from multi-hole probes has dramatically increased over the years (often better than quarter degree in the flow angles and half a percent in the velocity magnitude) has eliminated this theoretical approach as a viable candidate, especially for small probe sizes (1/8" tip diameter or smaller), where manufacturing imperfections are inevitable. For small probes, non-nulling methods are best suited. These methods are based on extensive calibration of the probe and allow for imperfections in the probe tip geometry. The probe is calibrated in a flowfield with known properties where the probe is rotated and pitched through a range of angles to simulate every possible flow incidence angle. At each angle combination, the port pressures are recorded and stored in a database. Some early work includes Gettelman and Krause [7], who determined the influence of the flow angle on static pressure

_____
This thesis follows the style of Journal of Fluids Engineering.

measurements in subsonic flowfields using a 2-hole wedge probe. Although they did not directly use it for angle predictions, they demonstrated the relationships that can be used for angle predictions. Centolanzi [8] used a 40-degree cone probe to determine the angle and speed in supersonic flows. He used an expression combining the measured pressures which would be sensitive to either the yaw or the pitch angle. Varying other parameters while maintaining the corresponding flow angle constant, would keep the expression fairly constant. Probe calibration is also discussed in Bryer and Pankhurst [1] where details on a probe traversing apparatus are presented. They gave a comprehensive overview of probe types, design, and construction as well as manometer systems for probes.

After the probe has been calibrated, the data is processed and sets of non-dimensional velocity-invariant coefficients are calculated that relate the relative magnitude of the port pressures to the flow incidence angle. Furthermore, these non-dimensional coefficients are typically curve-fitted to the angles to form explicit polynomial expressions (Rediniotis et al. [5]). Following the processing, the probe can be inserted into a flowfield with unknown velocity magnitude and angularity. The non-dimensional pressure coefficients are calculated from the port pressures and the flow angles are found directly from the polynomial expressions. A similar method is used to find the velocity.

There are a number of different approaches to the aforementioned procedure, varying in the definitions of the pressure coefficients and the method of curve fitting. Using only one set of coefficient definitions limits the angular range the probe can resolve since at high incidence angles the flow over one or more of the ports may be separated. Based on a 5-hole probe, Bryer and Pankhurst [1] divided the measuring region into a low-angle regime, corresponding to flow incidences resulting in the center port sensing the highest pressure, and four high-angle regimes, when one of the peripheral ports senses the highest pressure. This approach allows for region specific coefficient definitions and extends the angular range of the probe. Gerner and Maurer [9], Gerner and Sisson [10],

Everett et al. [11], [2] used 7-hole probes and split the angular domain into low-angle and high-angle flows similar to the methods by Bryer and Pankhurst [1], and extended the usable angular range up to 70 degrees in cone angle (angle between the velocity vector and the probe axis). Gerner and Maurer [9] defined separate non-dimensional pressure coefficients for the pitch and yaw angles. These coefficients were designed to be sensitive primarily to one of the two angles and not to the other. In other words, each one has a linear dependence on their respective angle and independence to the other angle. Also, like all pressure coefficients, these too are dependent upon Mach number and this becomes apparent only in the compressible regime (M > 0.3). As a corollary, the calibration data from any Mach < 0.3 can be used for the entire incompressible regime. Everett et al. [11], [2] determined the flow quantities with a set of third-order polynomial fits for each sector. They employed high speed computation to enable real-time flow measurement. They also investigated the effects of Reynolds number and found it to have no significant influence on the predicted flow properties. Kjelgaard [3] also measured the effects of Reynolds number by taking the calibration constants for the highest Reynolds number (from calibration data) and applying them to the data acquired for the lowest Reynolds number and vice versa. These data indicated little effect of Reynolds number in the measurements. Based on the work by Gerner and Maurer [9], Ostowari and Wentz [12] extended the angular range of a conical 5-hole probe to 85 degrees. However, no quantitative analysis of the errors in the high angle range was given.

The polynomial fitting of the non-dimensional coefficients to the flow angles has been studied extensively. Most early work used either a global procedure, where polynomials were created for all calibration points, or a sector based procedure (Gerner and Maurer [9]). Rediniotis et al. [5] were able to increase accuracy by dividing the port specific regions into several sections, thereby increasing the number of regions for which polynomials were used to describe the calibration coefficients. Houtman and Bannink [13] used a combined theoretical and experimental calibration on a hemispherical tipped

5-hole probe in high subsonic to supersonic flows. They found that the prediction capabilities were good at low flow angles, but deteriorated at cone angles larger than about 45 degrees due to separation and shock-wave effects. They also introduced a localized interpolation scheme using only eight calibration points for increased accuracy. Similar to the work by Houtman and Bannink [13], Zilliac [14], [4] and Johansen et al. [15] developed methods that are local in nature, where a calibration database is searched and interpolation or curve-fitting is performed locally, using only a few data points. Zilliac [14] used the Akima interpolation method, which is a weighted-nearest-neighbors method, instead of the more common (equally-weighted) curve-fit method and found significant reduction in errors. They also devised a simple technique to identify (and evade) pressure ports in the separated region of the 7-hole probe. Rediniotis and Vijayagopal [16] used Artificial Neural-Networks (ANN) rather than traditional polynomial fitting to relate the coefficient to the flow angles. Through extensive training, the ANN yielded very good prediction capabilities.

The definitions of the non-dimensional coefficients are crucial to maximizing sensitivity and data-reduction accuracy, minimizing dependence on Mach and Reynolds numbers, and avoiding singularities. Clark et al. [17] calibrated hemispherical tipped probes in high subsonic up to Mach 2.0 flows, examining five different calibration coefficient definitions for sensitivity to Mach number effects. They also compared ten identically produced probes and found that individual calibrations were required for each single probe due to manufacturing idiosyncrasies. Takahashi [18] performed analysis on the coefficient behavior identifying singularities while also optimizing for processing speed. Shepherd [19] introduced a 4-hole cobra probe with tip shape similar to a 5-hole probe, but with one central port and only three peripheral ports. Since there are only four independent quantities to be measured, the 4-hole probe avoids redundant (pressure) information. He calibrated and used this probe to resolve velocity and pitch and yaw angles with reasonable accuracy. However, he only used one set of coefficient definitions, which limited the angular range of the probe to +/- 20 degrees in pitch and

yaw. The maximum flow incidence angle that can be resolved by a 5- or 7-hole probe depends on the probe tip geometry and port locations. Most probes can accurately resolve angles up to approximately 70 degrees. For many complex flowfields, the angular range in the measurement domain (either spatially, temporally, or both) is greater than what a 5- or 7-hole probe can resolve (e.g. the flow in the wake of a bluff body), and for such flows the omni-directional probe (Fig. 1) is preferred (Kinser and Rediniotis [6]). The omni probe is an extension of the 5- and 7-hole probes with the distinct advantage that it can resolve flow angles up to 160 degrees from its principal axis. Similar to the 5-hole probe, the omni probe predicts the flow angles, the local total and static pressures, and the velocity magnitude with a high degree of accuracy.
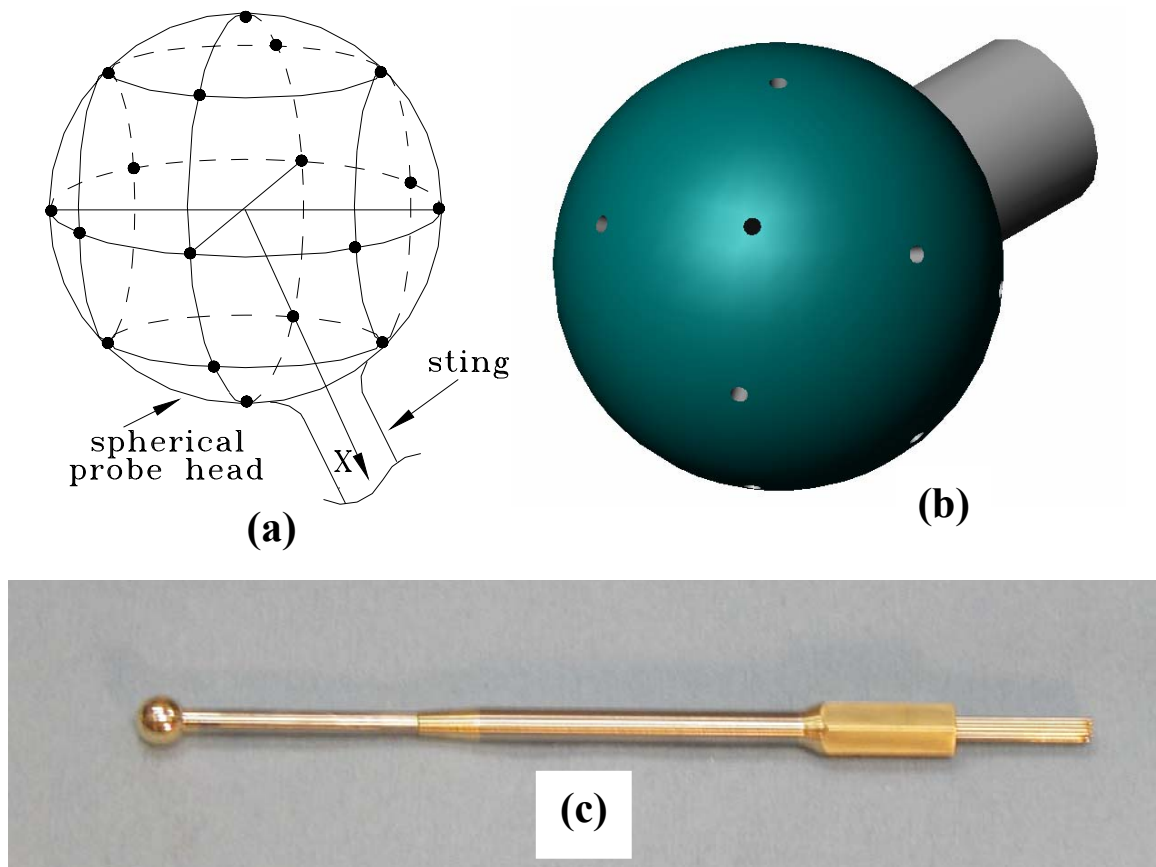
Fig. 1 Schematics and picture of the nearly omni-directional 18-hole probe: (a) port arrangement and grouping, (b) isometric view showing spherical tip and cylindrical sting and (c) photograph showing a fully assembled 18-hole probe.

The 12-hole probe developed here offers several advantages over the previously developed 18-hole probe. The new design has 12 pressure ports distributed on the surface of a spherical tip. Its 12 ports are located at the corners of an icosahedron (canonical shape with 20 sides - each one of which is an equilateral triangle - and 12 corners) inscribed inside a sphere (Fig. 2). The fact that the new design has 33% less number of holes has significant beneficial implications in the instrument's spatial resolution (smaller probe sizes become possible), frequency response (larger internal tubing diameters become possible) as well as cost of interfacing and usage.
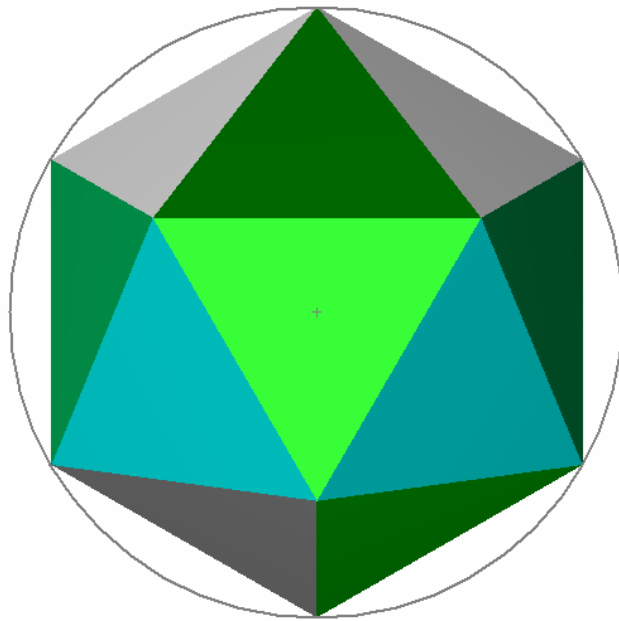
Fig. 2 Icosahedron inscribed inside a sphere. The ports are located at the 12 apexes of the icosahedron.

Consider for example two probes, an 18-hole and a 12-hole probe, both with the same spherical tip diameter, equal to 1/4" (0.25"). As seen in Fig. 1, all ports on the probe tip surface have to be routed to the base of the sting. Therefore, if the sting port/hole diameter is maintained the same for both probes, and equal to 0.014", the smaller the

number of ports, the smaller the minimum sting diameter necessary to accommodate them and thus the smaller the sting interference. This in turn leads to a larger measurable flow angularity. In our example, the resulting sting diameters are 0.10" and 0.09" for the 18-hole and 12-hole probes, respectively. As seen later, this reduced interference is also due to the fact that for the 12-hole probe, the tip surface ports closest to the sting are further from it than the ports closest to the sting in the 18-hole probe case. Alternately, if the sting diameter is maintained the same, for example equal to 0.10", the holes/ports in it can be made bigger in diameter for the case of the 12-hole probe, and can thus be interfaced with tubes of bigger inner diameter. This in turn can increase the measurement frequency response of the instrument (Rediniotis and Pathak [20]). In our example, the sting hole diameters for the 18-hole and 12-hole probes would be 0.014" and 0.016", respectively. Another possibility is, if one maintains the ratio sting diameter/tip diameter the same for both probes, as well as the same diameter for the sting ports, a smaller 12-hole probe can be manufactured, resulting in higher spatial resolution than the corresponding 18-hole probe, without sacrificing measurable angularity range or frequency response. Additionally, since every port has to be interfaced with a pressure sensor, significantly fewer pressure sensors are required for the operation of the 12-hole probe, resulting in fewer components and less expensive and/or complicated interface hardware. This advantage is accentuated, if the user plans to interface the probe with an ESP pressure scanner from PSI. The unit appropriate for this application would be either the 16-channel or the 32-channel unit (units with a number of channels between 16 and 32 are not available). For an 18-hole, a 32-channel unit would be necessary, while for the 12-hole probe, a 16-channel unit would suffice, resulting in 50% savings. Finally, reducing the number of ports from 18 to 12 results in reduction of the probe manufacturing time and thus probe price.

The reason for minimizing the tubing length is that any pressure-measuring instrument, such as the omniprobe, has a frequency response that is dependent upon the geometric parameters of the tubing system that connects the measurement point (at the tip of the

probe) to the transducer diaphragm and the properties of the medium in the tubing system. The longer the tubing, the poorer the frequency response. Moreover, we have developed the hardware and software necessary to correct for the effects of the tubing between the ports and the sensors. First, the frequency response curves (amplitude and phase) of the tubing system are obtained in an experimental facility we have developed and the results are also checked against theory. Once these are known, a numerical algorithm uses these response curves to reconstruct the true pressure signals (at the ports) from the measured signals (at the transducers).

The newly developed multi-hole probes (18-hole and 12-hole) do not necessarily have the conventional port arrangements of the 5- or 7-hole probes. One of the challenges when working with a generic port arrangement is that the conventional definitions of the non-dimensional pressure coefficients either can no longer be applied, or if they can be applied, they may be far from optimal. Some of the important properties of a properly defined coefficient include independence from the other three variables (for example, the yaw angle coefficient should be independent of the pitch angle, the dynamic and static pressures) and smooth, and preferably linear, behavior. As it will be demonstrated later, conventionally defined coefficients do not necessarily exhibit these properties for non-conventional port arrangements. There is therefore the need for a systematic way of defining well-behaved coefficients for any port arrangement. Additionally, several conventional definitions and data-reduction methods lack considerations of redundancy and fault tolerance. Simple examples are the typical definitions of the flow angle coefficients for a 5- or 7-hole probe in the low-angle regime. These definitions involve all 5 or 7 port pressures. Therefore, even if one of the 5 or 7 pressure sensors malfunctions, the conventional definitions fail, although the probe itself is still perfectly functional, at least in the low-angle regime, since only 4 ports are needed for the calculation of the flow quantities (two flow angles, total and static pressures).

This thesis presents a systematic way of defining well-behaved pressure coefficients for any generic port arrangement (5-, 7-, 12-, 18-hole or other) for spherical or hemispherical tipped probes. These definitions also take into account redundancy and fault-tolerance considerations. Then, a data-reduction algorithm for any generic port arrangement is developed. Finally the performance of the developed coefficients and data-reduction procedures is demonstrated for the 18-hole probe and the newly-designed 12-hole probe.

2   BASIC PRINCIPLE OF THE ALGORITHM

At any measurement point in the flow, the four quantities we are attempting to measure are: the two flow angles, the magnitude of the flow velocity U and the static pressure P_s. The flow angles are the angles that fully define the orientation of the local flow velocity vector with respect to the probe coordinate system $x_p y_p z_p$. These angles are the cone and roll angles Θ and Φ, as defined in Fig. 3. The other two angles defined in the figure, i.e. the pitch and yaw angles α and β, can, alternatively be used to describe the orientation of the velocity vector. Angles α and β can be expressed in terms of angles Θ and Φ and vice versa. The probe coordinate system, which will be referred to as the global coordinate system, is defined as follows: axis x_p is along the probe axis, from the tip to the probe base, while plane $x_p y_p$ is defined by a reference surface, which is one of the six flat surfaces of a hexagonal sleeve mounted at the back of the probe.

Let us consider 4 ports on the surface of the tip (taken as a sphere here) at arbitrary locations, as shown in Fig. 4. The ports are represented by the circles. As it will be discussed later, the locations of the ports cannot be totally arbitrary and there are some restrictions regarding their relative position in order to ensure that the four pressures measured by the ports can yield accurate estimates of the flow quantities of interest. Let us also assume that when the probe is positioned at a point in the flowfield it intends to measure, the stagnation point on the tip surface is point SP, represented by the star in Fig. 4. The center of the sphere is point C (not shown in the figure). Without loss of generality, let us assume that the ports are numbered according to the magnitude of the
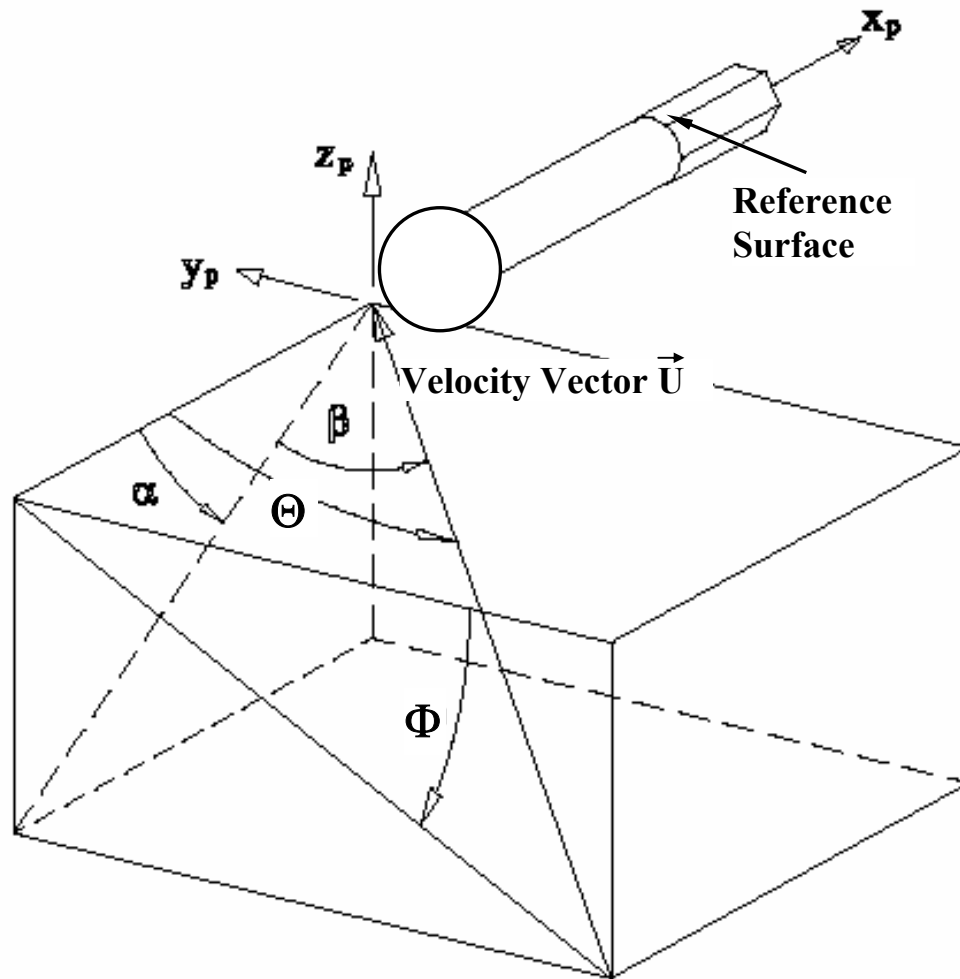
Fig. 3 Global coordinate system for the probe.

pressure they sense, i.e. port 1 measures the highest pressure and port 4 the lowest. The direction of the flow velocity vector is defined by the stagnation point SP and the center of the sphere. Since the positions of the four ports are fixed and known in the global coordinate system, the problem of finding the flow angles reduces to finding the location of the stagnation point SP in the local coordinate system, in terms of the angles θ, ϕ as defined in Fig. 4. Angle θ is the angle between lines C-SP and C-2, while angle ϕ is the angle between planes C-2-1 and C-2-SP.
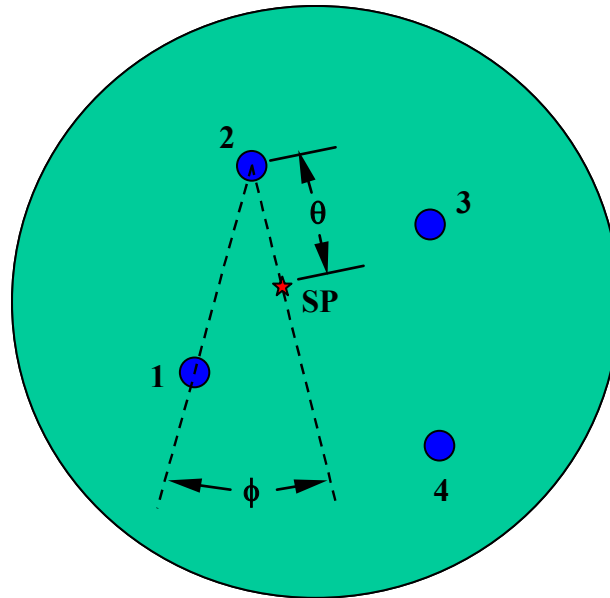
Fig. 4 Local coordinate system for the probe.

The pressures at the four ports can be written as:

$$P_i = P_s + q \cdot Cp_i \tag{1}$$

where P_s is the static (freestream) pressure, q is the dynamic pressure $(1/2)\rho U^2$, and Cp_i is the pressure coefficient at port i (i=1, 2, 3, 4). For the sake of illustration, assume potential flow with the surface velocity distribution give as:

$$u = (3/2) \cdot U \cdot \sin(\psi_i) \tag{2}$$

where U is the freestream velocity magnitude and angle ψ_i describes the position of port i with respect to the stagnation point SP and is the angle between lines C-SP and C-i, where i=1, 2, 3, 4. Then (1) can be written as:

$$P_i(\psi_i, U, P_s) = P_s + \frac{1}{2} \cdot \rho \cdot U^2 \left(\frac{9}{4} \cos^2(\psi_i) - \frac{5}{4} \right) \tag{3}$$

Since the geometric location of port i on the sphere is known, by applying simple geometric analysis we can easily show that the angle ψ_i is simply a function of the two unknown angles (θ, ϕ i.e. $\psi_i = \psi_i(\theta, \phi)$. For example, referring to Fig. 4, if (θ_3, ϕ_3) represent the coordinates of port 3 in the local coordinates reference system, then

$$\psi_3(\theta, \phi) = 2 \cdot \sin^{-1} \sqrt{\frac{1 - \cos\theta_3 \cdot \cos\theta - \sin\theta_3 \cdot \sin\theta \cdot \cos(\phi_3 - \phi)}{2}} \tag{4}$$

So, equation (3) can be written as:

$$P_i(\theta, \phi, U, P_s) = P_s + \frac{1}{2} \cdot \rho \cdot U^2 \left(\frac{9}{4} \cos^2(\psi_i(\theta, \phi)) - \frac{5}{4} \right) \tag{5}$$

We now have 4 equations (5) (for i from 1 to 4), and 4 unknowns (θ, ϕ, U, P_s) and can therefore solve for all 4 unknowns. We come to the same conclusion even if we relax our assumption of potential flow and consider viscous flow with a surface-velocity distribution (White [21]):

$$u = U \left(1.5 \cdot \psi_i - 0.4371 \cdot \psi_i^3 + 0.1481 \cdot \psi_i^5 - 0.0423 \cdot \psi_i^7 \right) \tag{6}$$

The above illustrates the basic principle of the algorithm. A few comments are in order here to ensure that the above equations can be uniquely solved for the flow unknowns. If we are to determine all four flow quantities (θ, ϕ, U, P_s), it is very important that all four ports are in the attached flow region. If only n ports are in the attached region (n<4), then only n out of the four unknowns can be determined. Moreover, for certain port arrangements, the possibility exists that there may be a stagnation point for which all angles ψ_i are equal, in which case not all four equations are independent of each other and therefore not all four unknowns can be determined. Also, if the highest three ports on the surface of the sphere are roughly "collinear", i.e. the three lines C-i, with i

corresponding to the three ports, are on the same plane, the algorithm's prediction was found to deteriorate. We will deal with both of these issues later.

If the probe tip was a perfect sphere and the port locations were accurately known, there would be no need for experimental calibration of the probe. The above theoretical analysis would be enough to yield, from the 4 measured port pressures (as long as all four ports are in the attached flow region), reasonably accurate answers for the flow velocity, angularity and static pressure. However, this is typically not the case. The probe tip is not a perfect sphere and probe machining imperfections (especially for small probe tip diameters) make it practically impossible to know exactly the port locations. The above necessitate probe calibration.

3   DESIGN OF THE NON-DIMENSIONAL PRESSURE COEFFICIENTS

One of the challenges when working with a generic port arrangement, not necessarily resembling the conventional 5-hole or 7-hole port arrangement pattern, is that the conventional definition of the non-dimensional pressure coefficients either can no longer be applied, or if it can be applied, it may be far from optimal. The previous statement is explained below.

It should be kept in mind here that two important properties of a properly defined coefficient are:

-   independence from the other three variables ([14]) (for example, the yaw angle coefficient should be independent of the pitch angle, the dynamic and static pressures).

-   smooth, and preferably linear, behavior.

Our experience with multi-hole probes has repeatedly demonstrated that a smooth and linear coefficient behavior is quite important for increased data-reduction accuracy (Rediniotis et al. [5]). Consider the two port arrangement patterns in Fig. 5. Fig. 5a shows a typical 5-hole port arrangement, while Fig. 5b shows a non-conventional port arrangement.
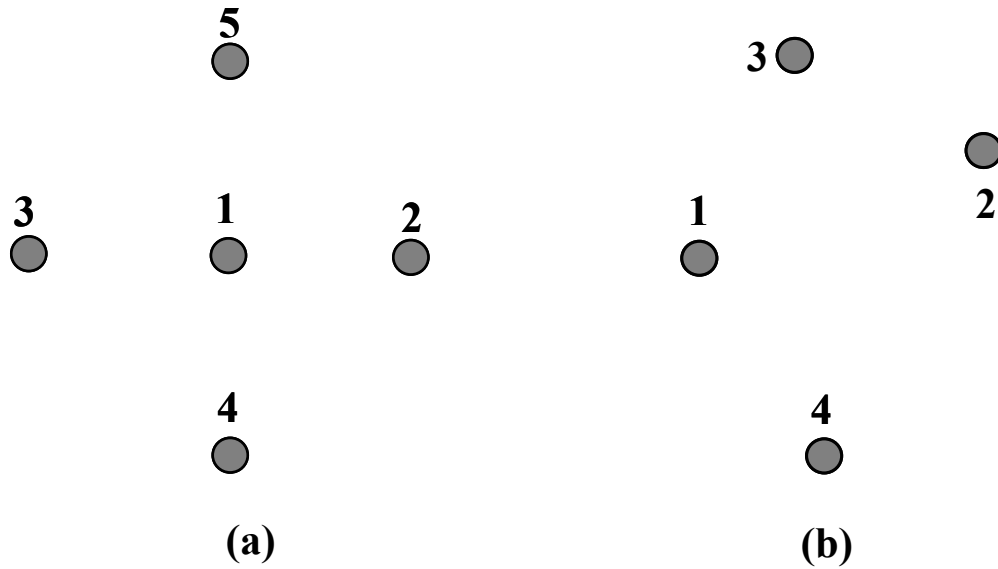
Fig. 5 Port arrangement: (a) conventional arrangement, (b) generic/non-conventional arrangement.

For the 5-hole arrangement, the yaw angle coefficient for low-angle flow (port 1 senses the highest pressure), for example, is typically defined as:

$$C_\beta = \frac{P_2 - P_3}{q_{est}} = \frac{P_2 - P_3}{P_1 - (P_2 + P_3 + P_4 + P_5)/4} \qquad (7)$$

which, due to the symmetry of the pattern, is intuitive and exhibits both of the properties stated above to a decent degree. However, for the non-conventional pattern of Fig. 5b, there is no obvious way to properly define a yaw angle coefficient. Even if one stretched the boundaries of intuition and defined the coefficient as:

$$C_\beta = \frac{P_3 - P_4}{q_{est}} = \frac{P_3 - P_4}{P_1 - (P_2 + P_3 + P_4)/3}, \qquad (8)$$

one would soon find that this coefficient does not have the desired properties we discussed above. For the purposes of design, theoretical pressure data for the 18-hole probe was generated based on equation (6) (viscous flow over a sphere). Fig. 6 shows the yaw angle coefficient, defined as in equation (8) above, for a typical sector in the 18-hole probe. As seen in the figure, the coefficient exhibits strong nonlinearity. Further, the

q_{est} defined above (equation (8)), which is supposed to be an estimate of the dynamic pressure and should thus be fairly constant for a fixed velocity magnitude and static pressure, regardless of flow angle, does not have the desired near-constant value, as shown in Fig. 7. The actual dynamic pressure for all the points in this figure is a constant equal to 61.25 Pa.
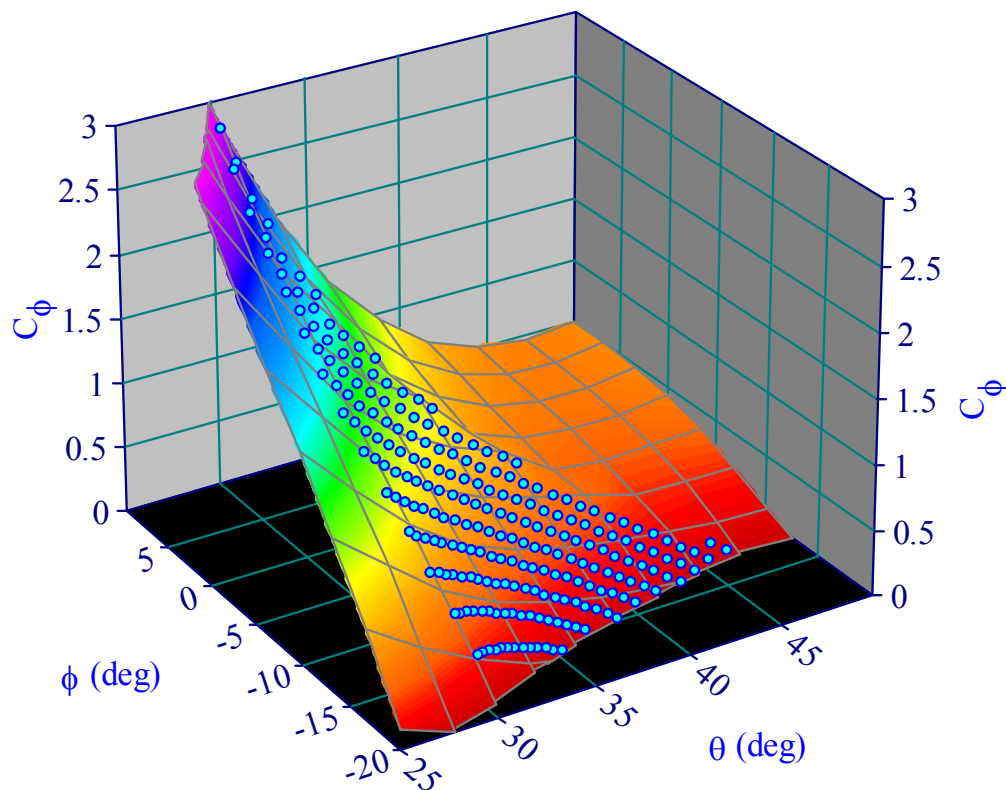
Fig. 6 Yaw angle coefficient defined conventionally in a sample sector of the 18-hole.
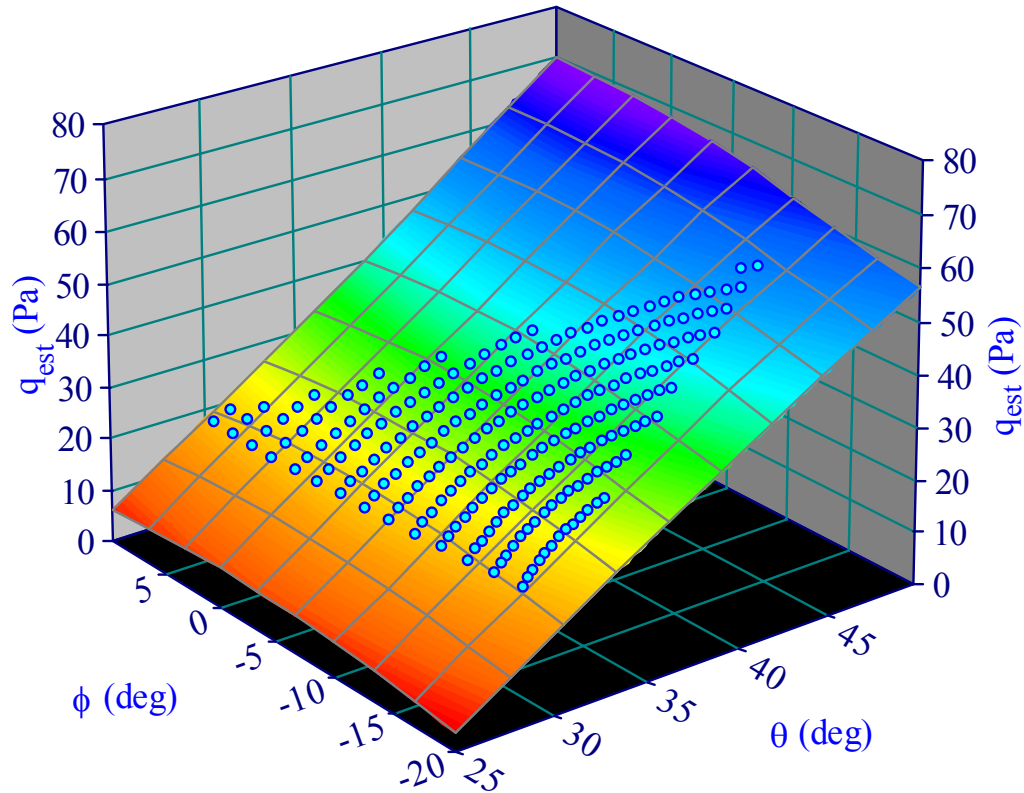
Fig. 7 Estimated dynamic pressure defined conventionally in a sample sector of the 18-hole.

Moreover, the way we went about defining the coefficient above is heuristic, and the definition is quite likely to change as the port pattern changes. The above discussion makes it obvious that a procedure is needed through which, for any non-conventional port arrangement, we can design the coefficients methodically such that they exhibit the desired properties. The procedure is described next.

Consider a multi-hole probe with a non-conventional port arrangement (such as the 18-hole or the 12-hole probe). First, the ports are numbered for identification of their location on the tip. The specific numbering scheme is not important, as long as it identifies the location of a port on the tip. Let us now assume that for a specific flow condition, the three ports that sense the highest pressures, in order of decreasing magnitude, have the numbers max1, max2 and max3 respectively. In the $\tilde{\Theta}\Phi$ domain

(see Fig. 3 for the definition of Θ, Φ), we define sectors pertaining to ports max1 through max3, as follows:

$$\text{SectorNumber} = \max1 \times 10^4 + \max2 \times 10^2 + \max3$$

As an example, Fig. 8 schematically presents the sector arrangement in the case where max1, max2, max3 take values from 1 to 5. In this figure, each sector is the locus of all possible stagnation points (in the Θ-Φ domain) that result in the order of the three highest pressures indicated by the number of the sector. For example, the triangle labeled "20103" is the locus of all possible stagnation points that result in port 2 sensing the highest pressure, and ports 1 and 3 sensing the second and third highest pressures, respectively. Each sector is only schematically represented as a triangle for simplicity. In reality, its boundaries are not necessarily straight lines. A local coordinate system is assigned to each sector as shown in Fig. 9 (same as that of Fig. 4).
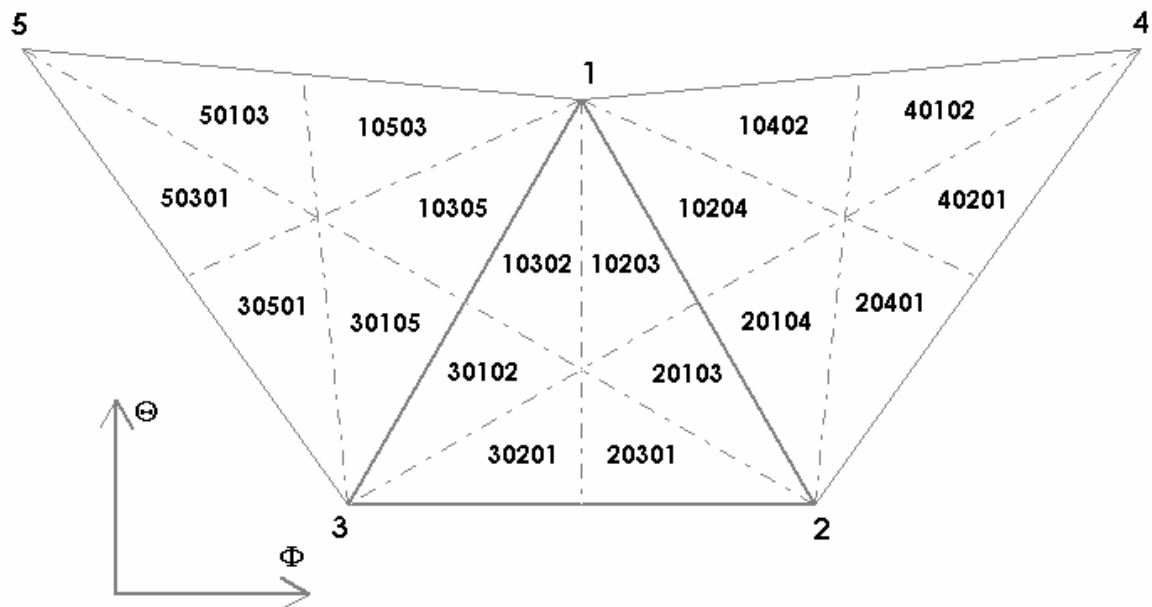
Fig. 8 Sector arrangement.
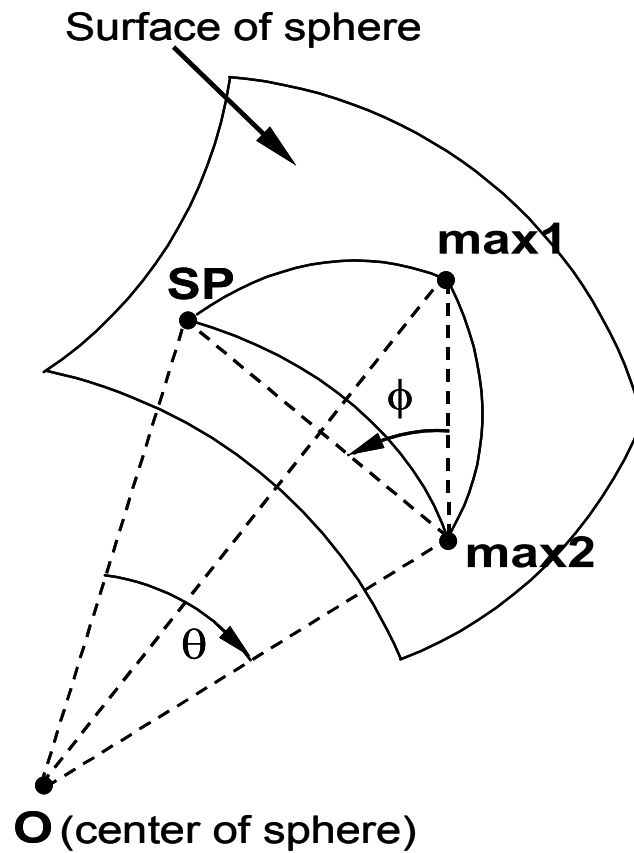
Fig. 9 Local coordinate reference system.

For each sector, the following procedure is followed in designing the coefficients. Let us consider sector 10203. For each stagnation point in the sector, the port with the fourth highest pressure is identified. The port with the most occurrences is labeled max4 for that sector. For example, for sector 10203: max4=4, for sector 30102: max4=5. Then, for all points in the sector (from the calibration database), the following linear surfaces/fits are generated:

$$\frac{\Delta P1}{q} = \frac{P_{max1} - P_{max3}}{q} = a1 + b1 \cdot \theta + c1 \cdot \phi \tag{9}$$

$$\frac{\Delta P2}{q} = \frac{P_{max2} - P_{max3}}{q} = a2 + b2 \cdot \theta + c2 \cdot \phi \tag{10}$$

$$\frac{\Delta P3}{q} = \frac{P_{max3} - P_{max4}}{q} = a3 + b3 \cdot \theta + c3 \cdot \phi \tag{11}$$

where θ, ϕ are the local stagnation point coordinates in radians, and a1, b1, c1, a2, b2, c2, a3, b3, c3, are (non-dimensional) constants determined by the least squares fitting. The numerator contains the difference of pressures in order to eliminate dependence on the static pressure (P_s) and is divided by the dynamic pressure (q) to eliminate dependence on q. It turns out that, for the 18-hole probe at least, these linear fits have very high correlation coefficients, (R^2 value) equal to or higher than 0.95. Subsequently, equations (9) and (10) are solved for θ, ϕ:

$$\theta = \theta_0 + A_\theta \cdot \frac{\Delta P1}{q} + B_\theta \cdot \frac{\Delta P2}{q} \tag{12}$$

$$\phi = \phi_0 + A_\phi \cdot \frac{\Delta P1}{q} + B_\phi \cdot \frac{\Delta P2}{q} \tag{13}$$

where the constants A_θ, B_θ, A_ϕ, B_ϕ are found by inverse transformation of equations (9) and (10). In equations (12) and (13), it is interesting to note that θ_0, ϕ_0 are the coordinates (in radians) of the stagnation point when $P_{max1} = P_{max2} = P_{max3}$. Then, the flow angle non-dimensional pressure coefficients C_θ and C_ϕ are defined as:

$$C_\theta = \theta - \theta_0 = \frac{A_\theta \cdot \Delta P1 + B_\theta \cdot \Delta P2}{q} \tag{14}$$

$$C_\phi = \phi - \phi_o = \frac{A_\phi \cdot \Delta P1 + B_\phi \cdot \Delta P2}{q} \tag{15}$$

The next challenge is to generate an estimate of the dynamic pressure that is as independent of (θ, ϕ as possible. The dynamic pressure (q_{est}) is expressed as:

$$q_{est} = R \cdot \Delta P1 + S \cdot \Delta P2 + T \cdot \Delta P3 \text{, or} \tag{16}$$

$$\frac{q_{est}}{q} = R \cdot \frac{\Delta P1}{q} + S \cdot \frac{\Delta P2}{q} + T \cdot \frac{\Delta P3}{q} \tag{17}$$

Plugging equations (9), (10) and (11) into (17), the constants R, S, and T are solved from the following system of three equations (by setting the coefficients of θ and ϕ equal to zero and the constant term equal to 1):

$$R \cdot a1 + S \cdot a2 + T \cdot a3 = 1 \tag{18}$$

$$R \cdot b1 + S \cdot b2 + T \cdot b3 = 0 \tag{19}$$

$$R \cdot c1 + S \cdot c2 + T \cdot c3 = 0 \tag{20}$$

The above equations force q_{est} to be equal to the actual q, and make it independent of the variables θ and ϕ. By plugging equation (16) in equations (14) and (15), the coefficients C_θ and C_ϕ can now be defined explicitly as:

$$C_\theta = \frac{A_\theta \cdot \left(P_{max1} - P_{max3}\right) + B_\theta \cdot \left(P_{max2} - P_{max3}\right)}{R \cdot \left(P_{max1} - P_{max3}\right) + S \cdot \left(P_{max2} - P_{max3}\right) + T \cdot \left(P_{max3} - P_{max4}\right)} \tag{21}$$

$$C_\phi = \frac{A_\phi \cdot \left(P_{max1} - P_{max3}\right) + B_\phi \cdot \left(P_{max2} - P_{max3}\right)}{R \cdot \left(P_{max1} - P_{max3}\right) + S \cdot \left(P_{max2} - P_{max3}\right) + T \cdot \left(P_{max3} - P_{max4}\right)} \tag{22}$$

Finally, the non-dimensional coefficients C_s and C_t for the static and total pressure are defined as:

$$C_s = \frac{P_{max1} - P_s}{q_{est}} = \frac{P_{max1} - P_s}{R \cdot \left(P_{max1} - P_{max3}\right) + S \cdot \left(P_{max2} - P_{max3}\right) + T \cdot \left(P_{max3} - P_{max4}\right)} \tag{23}$$

$$C_t = \frac{P_{max1} - P_t}{q_{est}} = \frac{P_{max1} - P_t}{R \cdot \left(P_{max1} - P_{max3}\right) + S \cdot \left(P_{max2} - P_{max3}\right) + T \cdot \left(P_{max3} - P_{max4}\right)} \tag{24}$$

The C_s and C_t definitions can be used irrespective of their dependence on flow angles, as long as they are velocity-invariant and single-valued. Note that the numerators in equations (23) and (24) are identical to those in traditional definitions of C_s and C_t.

The pressure data required for checking the designed coefficients can be either theoretically or experimentally (via probe calibration) generated. However, if the data used is theoretically generated, the "quality" of the designed coefficients will have to be ultimately tested with the experimental/calibration data. Experimental data, obtained via probe calibration, as described later, was also used to validate the quality of the designed coefficients. As an example, sector 10205 of the 18-hole is chosen to illustrate the behavior of the non-dimensional coefficients designed here. For this sector, the constants A_θ, B_θ, A_ϕ, B_ϕ, R, S and T are found to be 0.330, -0.272, -0.450, -0.658, 1.074, 1.128 and 1.037, respectively, based on theoretically generated data. The port pressures (hence

P_{max1}, P_{max2} etc.) and P_s, P_t (flow conditions) at different (θ, ϕ) locations within the sector are known. Hence the four coefficients in equations (21), (22), (23) and (24) and also q_{est} in equation (16) can be plotted for the sector as functions of the local (θ, ϕ).

Fig. 10a and Fig. 11a present plots of $C_\theta(\theta,\phi)$ and $C_\phi(\theta,\phi)$, respectively, based on theoretical data. To show that the coefficients designed with theoretically generated data behave in the same way when applied to the actual (experimentally generated) calibration data, Fig. 10b and Fig. 11b present plots of $C_\theta(\theta,\phi)$ and $C_\phi(\theta,\phi)$, respectively, for the same sector, with experimental calibration data. For this case, the constants A_θ, B_θ, A_ϕ, B_ϕ, R, S and T were found to be 0.361, -0.390, -0.595, -0.513, 1.176, 0.996 and 1.146, respectively (versus 0.330, -0.272, -0.450, -0.658, 1.074, 1.128 and 1.037, for the theoretically generated data). It is clear that the experimental surfaces have the desired qualities/properties and behave similar to the theoretical data. It should be stressed here that the viscous sphere pressure-distribution equation (6) is used only with the intention of studying the newly-designed non-dimensional probe coefficients. For the actual probe calibration and reduction, the pressure data is obtained experimentally and used exclusively, as explained in the next sections. As seen in Fig. 10 and Fig. 11, both for theoretical and experimental data, and contrary to the behavior of the conventional coefficient definition represented in Fig. 6, it is clear that $C_\theta(\theta,\phi)$ demonstrates smooth and linear behavior and good independence from ϕ, while $C_\phi(\theta,\phi)$ demonstrates smooth and linear behavior and good independence from θ. As explained earlier, both C_θ and C_ϕ are, by definition, independent of P_s and q. This means that the calibration data obtained at some flow conditions (P_s, q) can be used for all flow conditions (within a reasonable Mach number range, typically of +/-0.1).
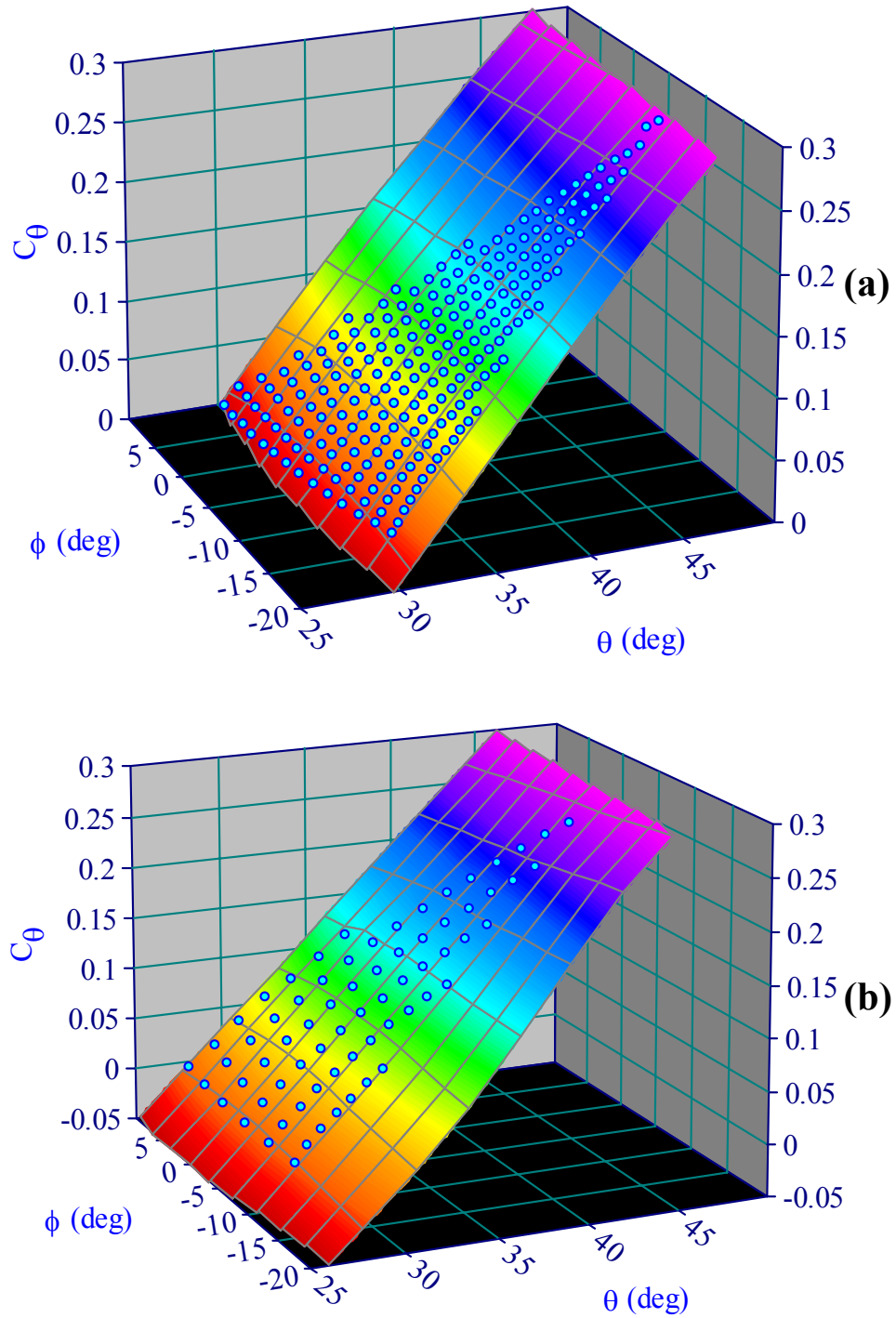
Fig. 10 Typical behavior of the newly-defined cone angle coefficient (equation 21) for the 18-hole probe: (a) theoretical data, (b) experimental calibration data.
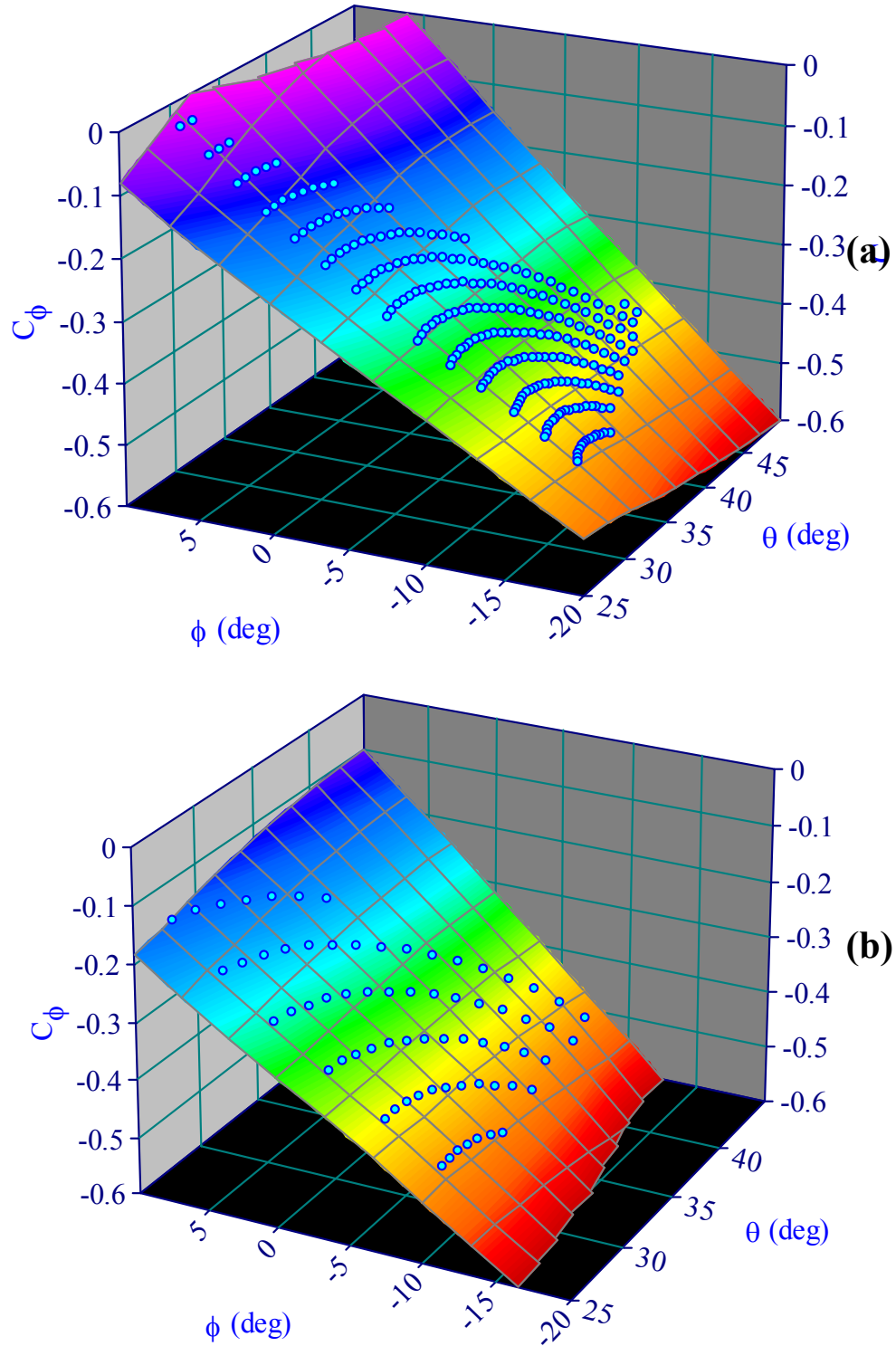
Fig. 11 Typical behavior of the newly-defined roll angle coefficient (equation 22) for the 18-hole probe: (a) theoretical data, (b) experimental calibration data.

Fig. 12 presents a plot of $q_{est}(\theta,\phi)$ obtained with theoretical pressure data. The actual dynamic pressure for all the points here is, as before, 61.25 Pa. It is clear that $q_{est}(\theta,\phi)$ demonstrates smooth and nearly constant behavior (especially as compared to that of Fig. 7) and independence from θ, ϕ. Fig. 13 and Fig. 14 present plots of C_s and C_t, respectively, (again, with theoretical data) illustrating well-behaved surfaces.
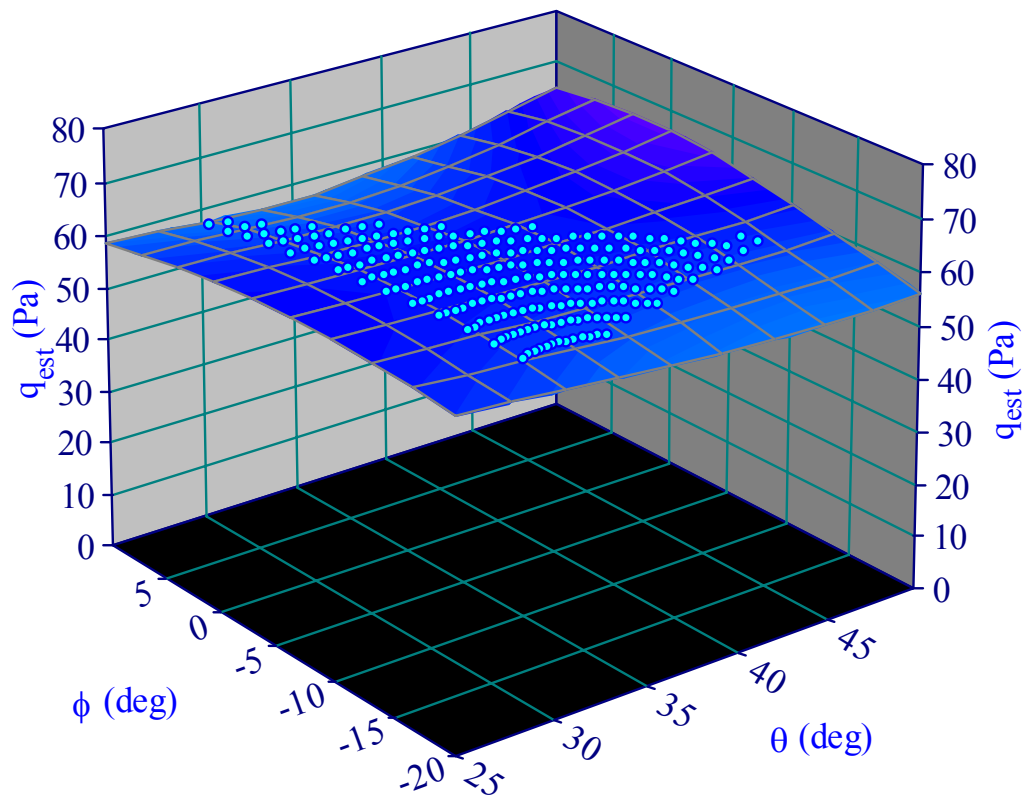
Fig. 12 Typical behavior of the newly-defined estimated dynamic pressure (equation 16).

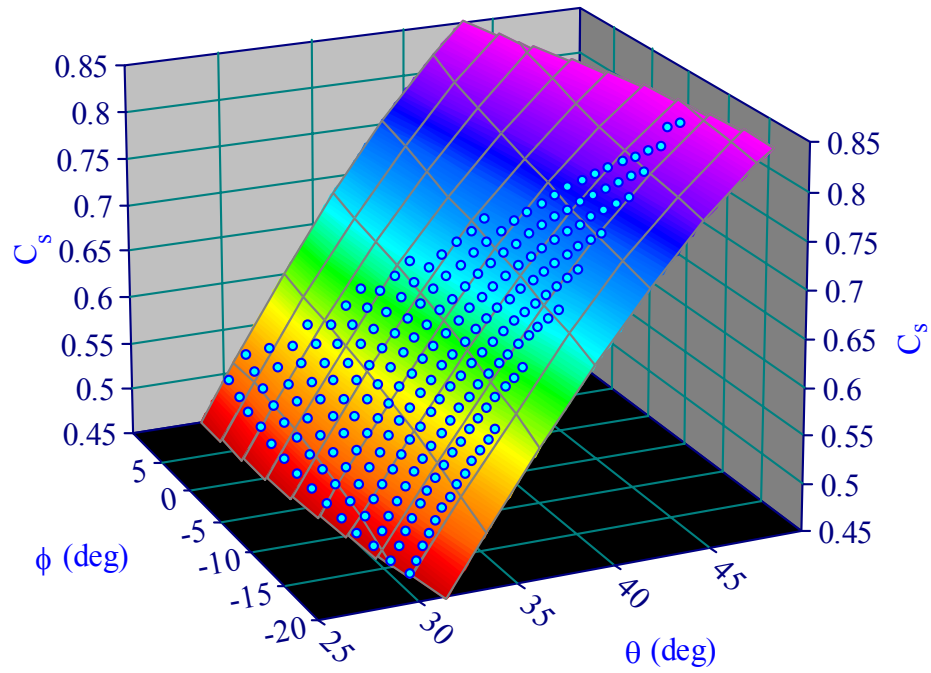**Fig. 13 Typical behavior of the newly-defined static pressure coefficient (equation 23).**
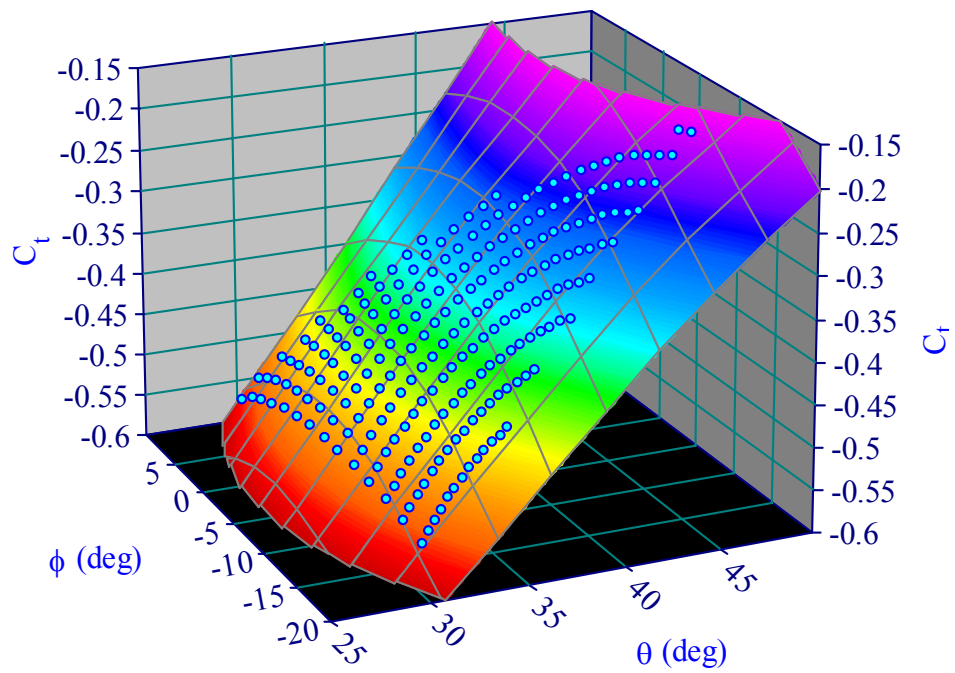

**Fig. 14 Typical behavior of the newly-defined total pressure coefficient (equation 24).**

4   PROBE CALIBRATION

A typical 18-hole probe with a tip diameter of 0.25 in. was calibrated in a high-speed wind tunnel, at different Mach numbers: 0.05, 0.1, 0.2, 0.3, 0.4, 0.5, 0.6 and 0.7. The experimentally obtained calibration database of the 18-hole probe consists of all 18 port pressures and the freestream dynamic pressure for a wide range of flow angles. The cone angle Θ was varied from 0 deg to about 150 deg in steps of 1.8 deg. For each one of these cone angles, the roll angle Φ was varied from -180 deg to 180 deg in steps of 3.6 deg. Thus a total of about 8000 calibration points (stagnation point locations) all around the probe tip (except near the sting) are available. The probe was mounted on a dual-axis stepper-motor assembly, which can vary the cone and roll angles (Θ, Φ) through the desired range stated above. At each of the probe orientations the 19 pressures were acquired with a 32-transducer electronic pressure scanner (ESP) from PSI, Inc. An ESP unit with a pressure range of ± 10 in. H_2O was used for the M = 0.05 and the M = 0.1 calibrations, a ± 20 in. H_2O unit was used for the M = 0.2 calibration, and a ± 10 psi unit was used for all of the other calibrations. At each probe orientation, 1 second was allowed for the flow to settle and then measurements were taken for 4 seconds at 256Hz with a 12-bit data acquisition board. The wind-tunnel generates a jet out of a nozzle, 1" × 2" (2.5 cm × 5 cm) in dimensions and can attain a maximum speed of 320 m/s with a freestream turbulence of less than 0.25%.

5 PREPROCESSING THE CALIBRATION DATA

First, the data in the calibration database is allocated among all the sectors and transformed into the respective local coordinate systems. Then the coefficients A_θ, B_θ, A_ϕ, B_ϕ, R, S and T for each of the sectors, as described in the previous sections, are calculated. Only those sectors with at least 5 calibration points within them are chosen as valid. The points lying in any of the discarded sectors are reassigned to adjacent sectors. Also, if the highest three pressure ports are found to be "collinear" as described earlier, $\Delta P3$ in equation (11) can be redefined as ($P_{max2} - P_{max4}$) and was found to work well. Alternately, the third highest pressure port could be discarded and another port before the separation region (if available) can be selected. The second technique was used for the 18-hole probe since there was always an extra port available. In the 12-hole, such a situation due to the arrangement of ports was never encountered. Then, for each calibration point, the non-dimensional coefficients (C_θ, C_ϕ, C_s and C_t) and the stagnation point coordinates (θ, ϕ), in the local reference system, as described in Fig. 9, are calculated. To calculate the latter, it is necessary to have at least an estimate of the coordinate locations of the pressure ports. Due to the inevitable deviation from the design port location while machining, these have to be estimated based on the pressures from the calibration database. The pressure at any port due to the nearest few stagnation points behaves as shown in Fig. 15. By fitting a quadratic surface through the points and finding the (Θ, Φ) corresponding to the local maximum, a good estimate of the port's coordinate location can be obtained.
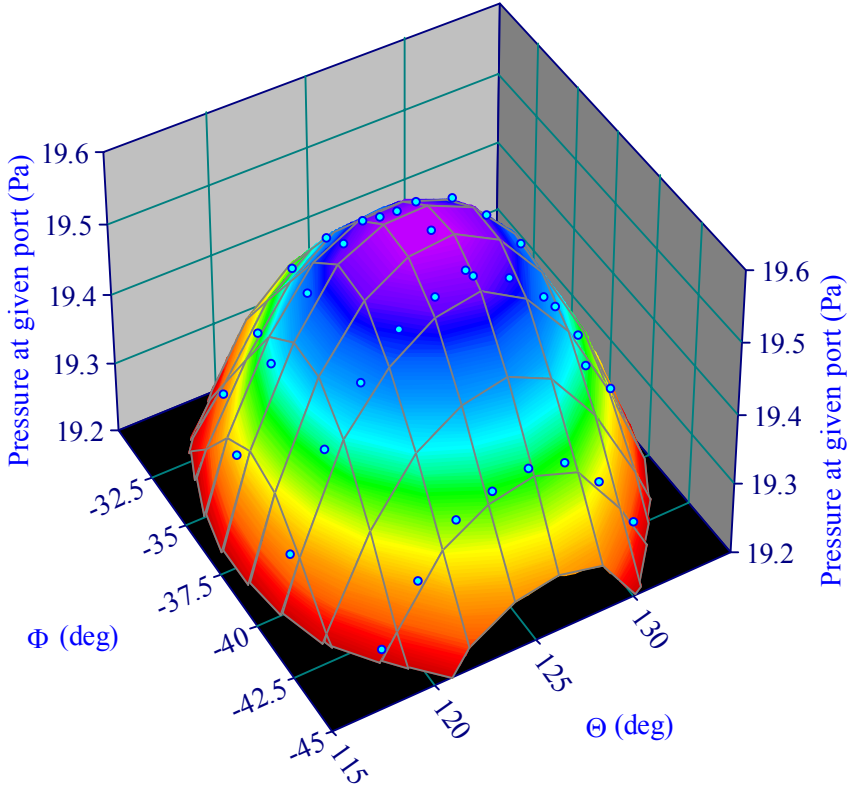
Fig. 15 Pressure at port#2 of an 18-hole probe, varying with the stagnation point location (or equivalently, the flow angles).

6   DATA REDUCTION

During an actual application of the probe, the following procedure is followed to calculate the flow variables, which consist of the two flow angles, the static and total pressure. For a given measurement data point, all port pressures are measured. Based on the highest three pressures, the sector number and the corresponding coefficients for the sector are obtained. At this point the algorithm checks if the sector number obtained is valid (i.e., sector is existent). If the sector number is found as one that was removed during preprocessing due to insufficient number of points within it, then the current test point is assigned to a suitable adjacent sector. The reader should recall that during the coefficient designing procedure (previous section), we generated seven coefficients, A_θ, B_θ A_ϕ, B_ϕ, R, S, T, for each sector, unique to each sector, which are used in defining the non-dimensional coefficients C_θ, C_ϕ and the estimated dynamic pressure q_{est}. Using these coefficients, C_θ and C_ϕ are calculated for the data point. $C_{\theta\text{-CAL}}$ and $C_{\phi\text{-CAL}}$ for the adjacent calibration points are obtained from the preprocessed calibration database. From these, the closest 30 calibration points are selected, based on their Euclidean distance (d) from the current (C_θ, C_ϕ):

$$d = \sqrt{(C_\theta - C_{\theta-CAL})^2 + \lambda \cdot (C_\phi - C_{\phi-CAL})^2} \qquad (25)$$

The scaling factor λ is introduced in the above equation to bring both the coefficients to the same scale and is defined for every sector based on the maximum and minimum values of its coefficients:

$$\lambda = \frac{(C_\theta)_{max} - (C_\theta)_{min}}{(C_\phi)_{max} - (C_\phi)_{min}} \qquad (26)$$

To properly deal with data points that might be very close to the boundaries of a sector, calibration points from 10 adjacent sectors are also considered. For example, if the data point is in sector 10203 (see Fig. 8), calibration points from sectors 10204, 20103 and

10302 and so on are also used. The selected points are distributed into 4 quadrants in the C_θ-C_ϕ plane with the data point's (C_θ, C_ϕ) as the origin. This is done so as to ensure that the selected calibration points "enclose" the test point. Out of the points thus distributed the nearest one from each quadrant is selected, one quadrant after the other, until the required number of calibration points (m) is obtained. Least-squares surface fits are performed locally on the selected calibration points for all the four variables. Subsequently these fits are used to calculate the quantities θ, ϕ, C_s and C_t corresponding to the current data point (C_θ, C_ϕ). A quadratic fit with m = 8 is seen to produce the best results. The θ, ϕ calculated are converted to global coordinates to get the global flow angles Θ, Φ. Then, the static and total pressures (P_s, P_t) are calculated from:

$$P_s = P_{max1} - C_s \cdot q_{est} \tag{27}$$

$$P_t = P_{max1} - C_t \cdot q_{est} \tag{28}$$

Using adiabatic, prefect gas relationships for air, the Mach number and static temperature (T_s) are calculated:

$$M = \sqrt{5\left(\left(P_t / P_s\right)^{2/7} - 1\right)} \tag{29}$$

$$T_s = \frac{T_t}{1 + M^2 / 5} \tag{30}$$

The freestream velocity magnitude is then arrived at by the equation:

$$U = M \cdot \sqrt{\gamma \cdot R \cdot T_s} \tag{31}$$

Finally, the velocity components in the probe (global) coordinate system are calculated:

$$
\begin{aligned}
U_x &= U \cdot \cos \Theta \\
U_y &= U \cdot \sin \Theta \cdot \cos \Phi \\
U_z &= U \cdot \sin \Theta \cdot \sin \Phi
\end{aligned} \tag{32}
$$

The flowchart in Fig. 16 illustrates the data reduction process.
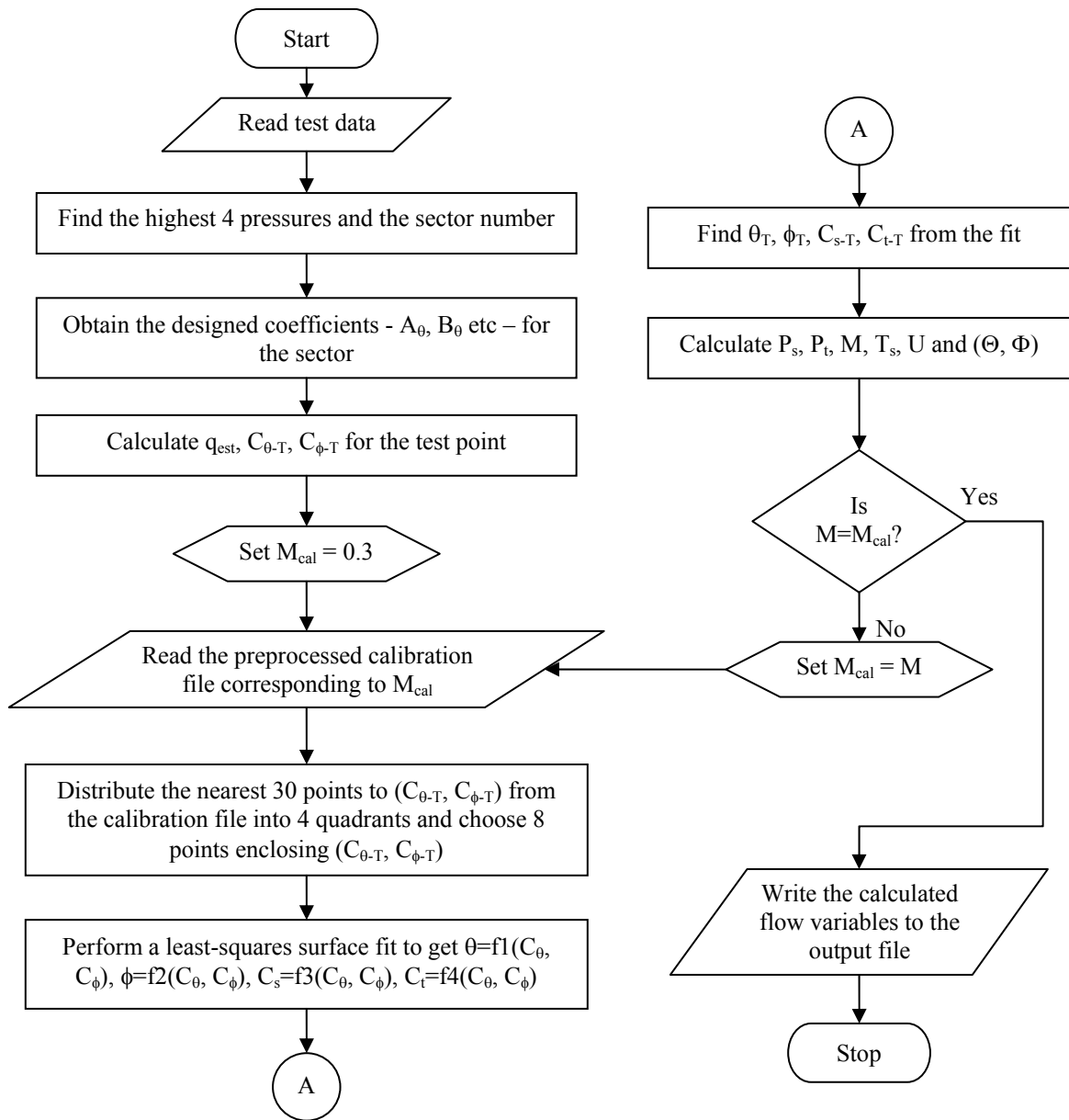
Fig. 16 Data reduction process.

In order to account for Mach number effects, a probe is typically calibrated in a range of Mach numbers, in steps of 0.1 in the Mach number (for example at Mach: 0.1, 0.2, 0.3, etc.), thus generating several calibration files/databases, one per Mach number. When the probe is used in an unknown flowfield, since the Mach number at the measurement location is not known, it is unknown which calibration file/database to use for the data

reduction of the specific point. Therefore, since during data reduction it is necessary to arrive at the correct calibration file, which corresponds to the flow Mach number, an iterative scheme is adopted. If the calibration file used for data reduction corresponds to a Mach number quite different from that of the measurement point, the predicted results can be highly erroneous. For example, the percentage error in the velocity magnitude for a flow at Mach 0.2 reduced with calibration data from Mach 0.5 was found to be as much as 6%. Although this is high, it serves to obtain a very good initial estimate of the measurement point's Mach number (0.2 in this case). Therefore, for the first iteration, one can reduce the test data with, say, the Mach 0.3 calibration database and estimate the Mach number of the flow. Then a second iteration can be performed with the calibration database nearest to this estimated Mach number. We have implemented this procedure with conventional multi-hole probes, with very good results ([15]).

7   RESULTS AND DISCUSSION

The algorithm was coded in Matlab 6.1 and in its present state can reduce 250 points per second (in a 2.4 GHz, 512 MB RAM Pentium-Class computer). Efforts are underway to write the code in Delphi (Pascal-based) to attain a faster reduction capability and a user-friendly GUI. The reduction code was tested with the calibration data for the 18-hole probe. The calibration data itself was used as test data. It was made certain that for every test point, its own data was removed from the calibration data during reduction. The data consisted of 7400 test points obtained at a Mach number of 0.2 with the Θ-coordinate ranging up to 145 deg. Very accurate predictions were attained for the predicted flow angles, the velocity magnitude, the static and total pressures. Fig. 17 and Fig. 18 present the individual error histograms for the flow angles in the global reference system (Θ and Φ). Fig. 19 shows the histogram of the error (in percent) for the freestream velocity magnitude (U). The percent errors, taken with respect to the freestream dynamic pressure (q), in the predicted static and total pressures (P_s and P_t) are shown in Fig. 20 and Fig. 21. In all these plots, Gaussian error distributions are observed, with means very close to zero, which shows that there were no bias errors in the calibration or data-reduction processes.
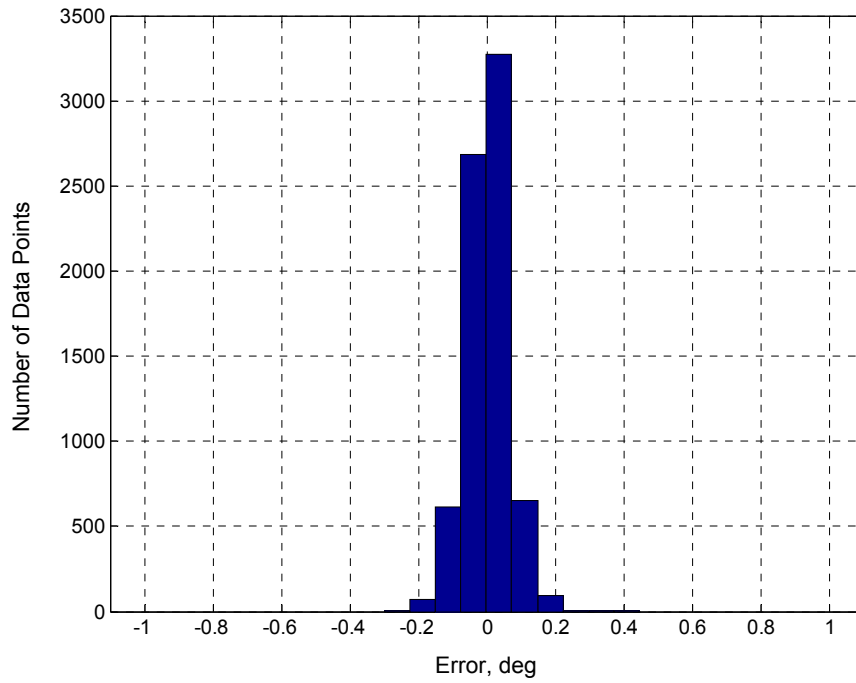
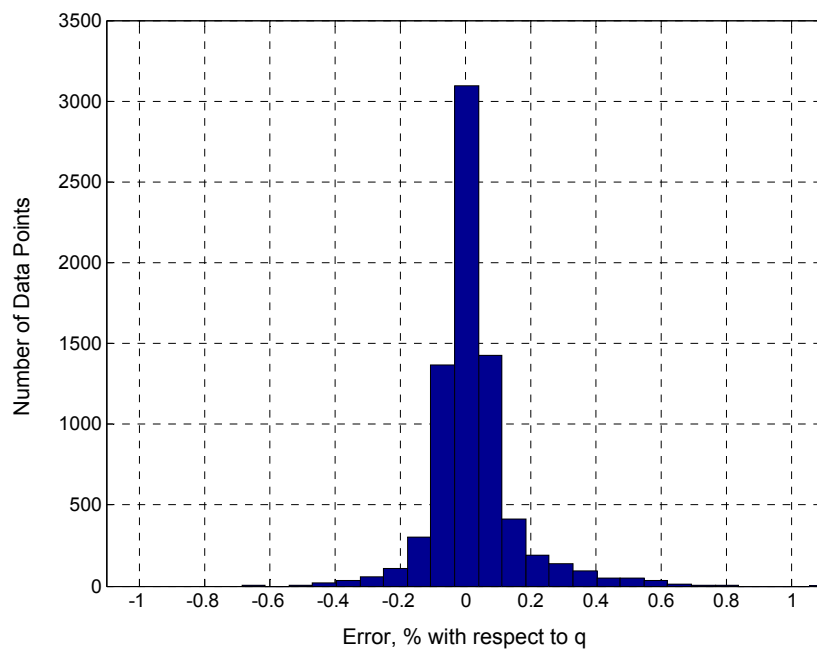**Fig. 17 Histogram of the error in the predicted cone angle (Θ) in degrees.**
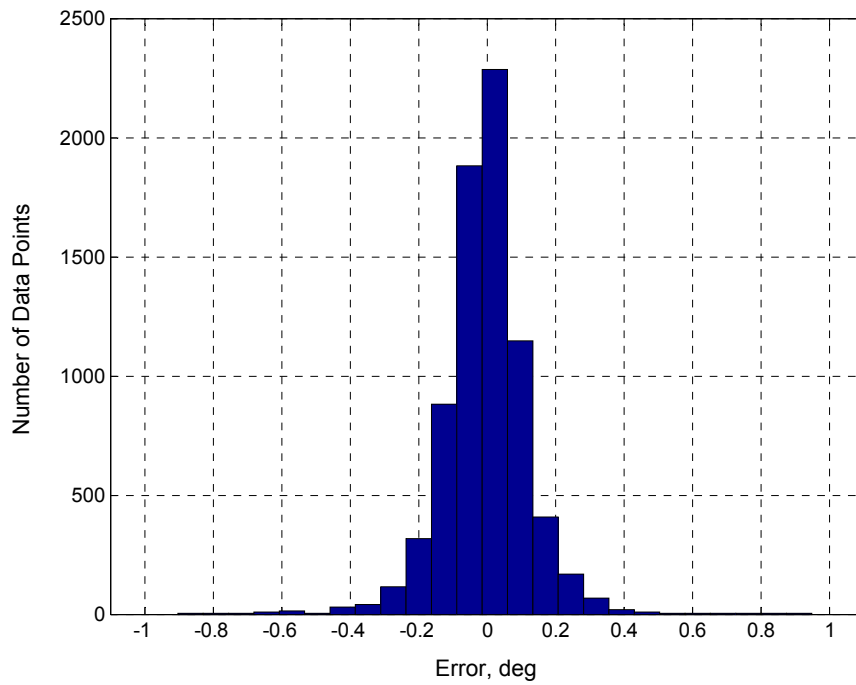
Fig. 18 Histogram of the error in the predicted roll angle (Φ) in degrees.
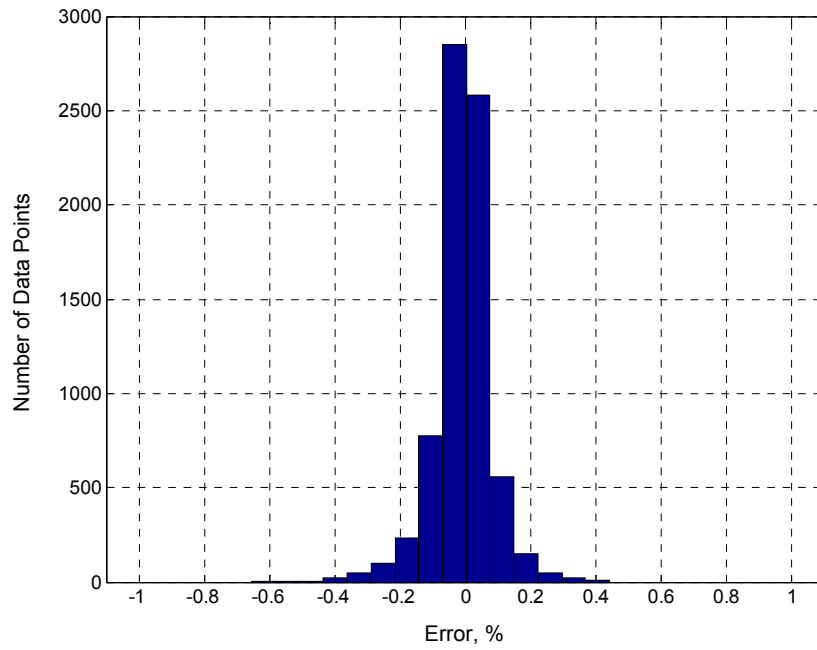
Fig. 19 Histogram of the percentage error in the predicted velocity magnitude (U).

Fig. 20 Histogram of the error in the predicted static pressure (P$_s$) as a percentage of dynamic pressure (q).
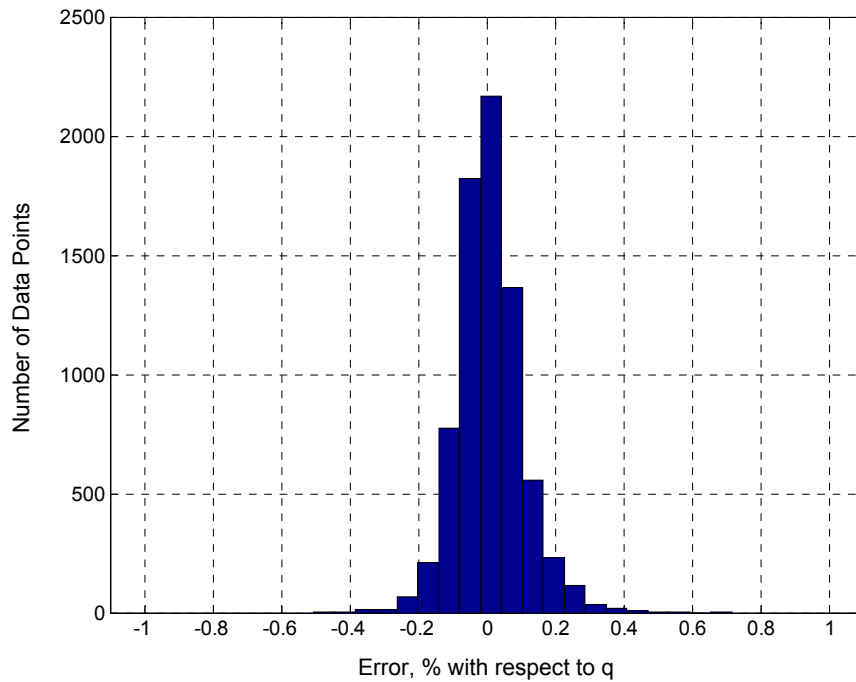
Fig. 21 Histogram of the error in the predicted total pressure (P_t) as a percentage of dynamic pressure (q).

Table 1 shows the statistical data from the error analysis. It should be born in mind that these results were obtained with a handicap, i.e., for every test point, the test point itself was not part of the calibration points used for data reduction. This results in larger Euclidean distances between the test point and the nearest calibration points, as compared to the case in which the test points are at intermediate locations. Yet, very good predictions are observed as seen from the small standard deviations. For example, for the error in Θ (Table 1), a standard deviation of 0.061 deg. means that about 68% of the predictions will have an error (compared to the exact Θ angle) less than or equal to 0.061 deg., or about 95% of the predictions will have an error less than or equal to 2 × 0.061 deg. = 0.122 deg.

Table 1. Error data for the predicted variables at M=0.2.

	Maximum	Mean (μ)	Standard Deviation (σ)
Error in Θ (deg)	0.444	0.002	0.061
Error in Φ (deg)	0.946	-0.004	0.122
Error% in U	0.654	-0.008	0.086
Error% in P_s w.r.t q	1.127	0.024	0.128
Error% in P_t w.r.t q	0.713	0.008	0.096

To check for consistency, the reduction was performed for the same probe at Mach numbers of 0.05, 0.1, 0.3, 0.4, 0.5, 0.6 and 0.7. For each case, the coefficients were designed specifically for that Mach number from their respective calibration data. In all these cases, the means and standard deviations are very similar to the Mach 0.2 case. Table 2 and Table 3 show the error data at Mach 0.05 and 0.7 respectively. The higher maximum errors in the Mach 0.7 case is due to a few stray bad points and is not of much concern.

Table 2. Error data for the predicted variables at M=0.05.

	Maximum	Mean (μ)	Standard Deviation (σ)
Error in Θ (deg)	0.548	0.001	0.081
Error in Φ (deg)	1.324	-0.004	0.162
Error% in U	0.615	-0.010	0.130
Error% in P_s w.r.t q	1.392	0.024	0.150
Error% in P_t w.r.t q	1.024	0.004	0.201

Table 3. Error data for the predicted variables at M=0.7.

	Maximum	Mean (μ)	Standard Deviation (σ)
Error in Θ (deg)	0.598	0.001	0.061
Error in Φ (deg)	1.210	0.001	0.131
Error% in U	1.311	-0.002	0.130
Error% in P_s w.r.t q	1.706	0.013	0.188
Error% in P_t w.r.t q	1.054	0.012	0.097

Since the sector coefficients A_θ, B_θ, A_ϕ, B_ϕ, R, S and T were designed to be independent of the freestream dynamic pressure, a test was performed to use these coefficients obtained from the pressure data at one Mach number and applied to the reduction at another Mach number. Table 4 shows the results obtained by using the sector coefficients at Mach 0.7 in calculating the flow variables at Mach 0.2. As expected, the error data behaves similar to that in Table 1.

**Table 4. Error data for the predicted variables at M=0.2 with sector coefficients from M=0.7.**

|	Maximum	Mean (μ)	Standard Deviation (σ)
Error in Θ (deg)	0.423	-0.003	0.059
Error in Φ (deg)	1.136	-0.005	0.135
Error% in U	0.512	-0.002	0.081
Error% in P_s w.r.t q	0.870	0.013	0.111
Error% in P_t w.r.t q	0.631	0.010	0.102

8   DESIGN OF THE 12-HOLE PROBE

The new design has 12 pressure ports distributed on the surface of a spherical tip. Its 12 ports are located at the corners of an icosahedron (Fig. 2), inscribed inside a sphere. The CAD model of the prototype 12-hole probe is shown in Fig. 22 and Fig. 23. The main difference between the two figures is the location of the sting on the spherical tip. In Fig. 22, the center of the sting is located at the geometric center of any two adjacent ports; while in Fig. 23, the center of the sting is located at the geometric center of any three adjacent ports. These two configurations will be referred to as the two-port and the three-port sting configuration, respectively. The importance of sting location will be discussed a little later. In both configurations, the locations of the tip ports are described in a spherical coordinate system, as defined in Fig. 3. For the two-port and three-port sting configurations, the locations of the tip ports are given in Table 5 and Table 6 respectively, in terms of their Θ and Φ coordinates.

For the two-port sting configuration, Fig. 22 presents a perspective view of the tip (Fig. 22a), and front, side and back views of the tip (Fig. 22b, Fig. 22c, Fig. 22d respectively), illustrating the location and numbering of the ports. Although ports 7 and 8 are not shown, port 7 is located diametrically opposite to port 5 and port 8 is located diametrically opposite to port 6. Fig. 22d also illustrates the arrangement of the holes on the base of the sting.
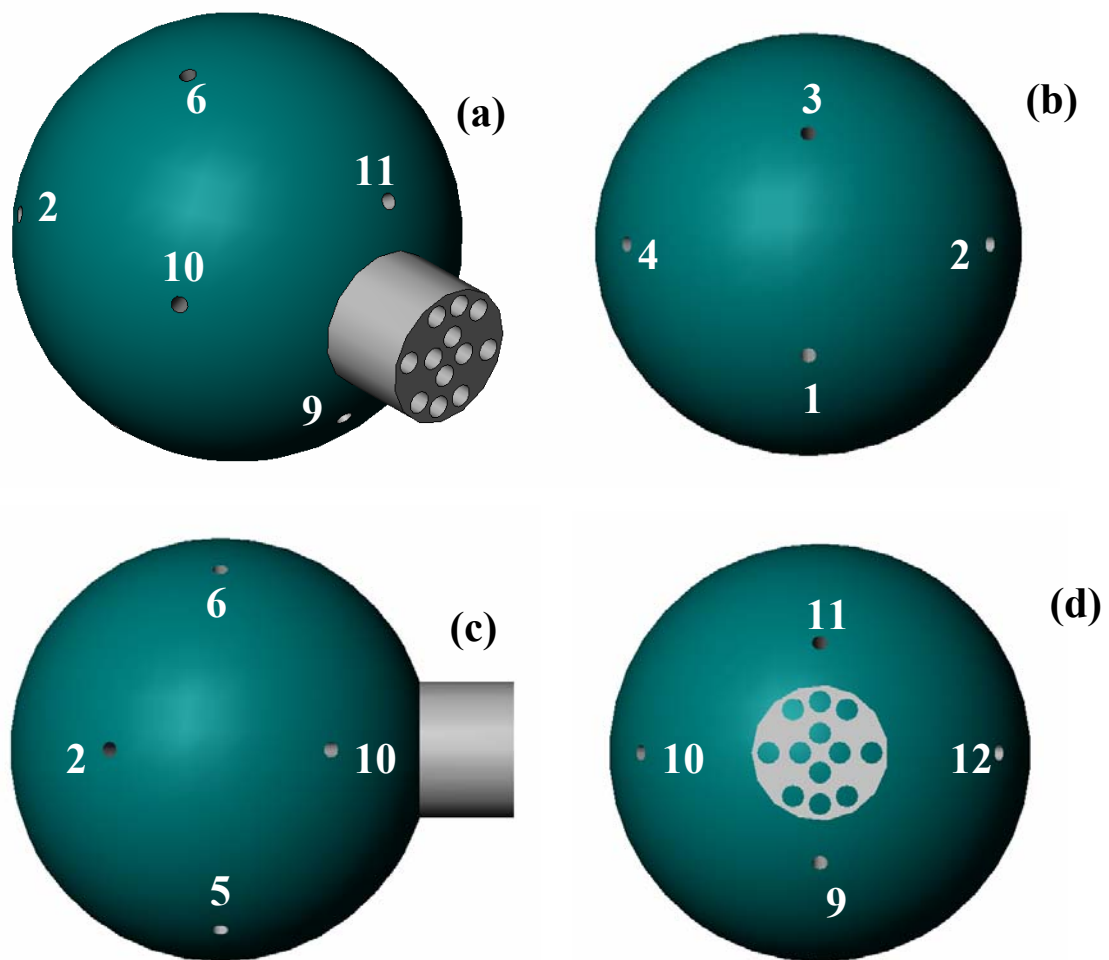
Fig. 22 Model of 12-hole probe for the two-port sting configuration: (a) perspective view, (b) front view, (c) side view, (d) back view. Probe tip diameter: 3/8", ratio of sting diameter over probe diameter: = 0.324, tip hole diameter: 0.014", sting hole diameter: 0.020".
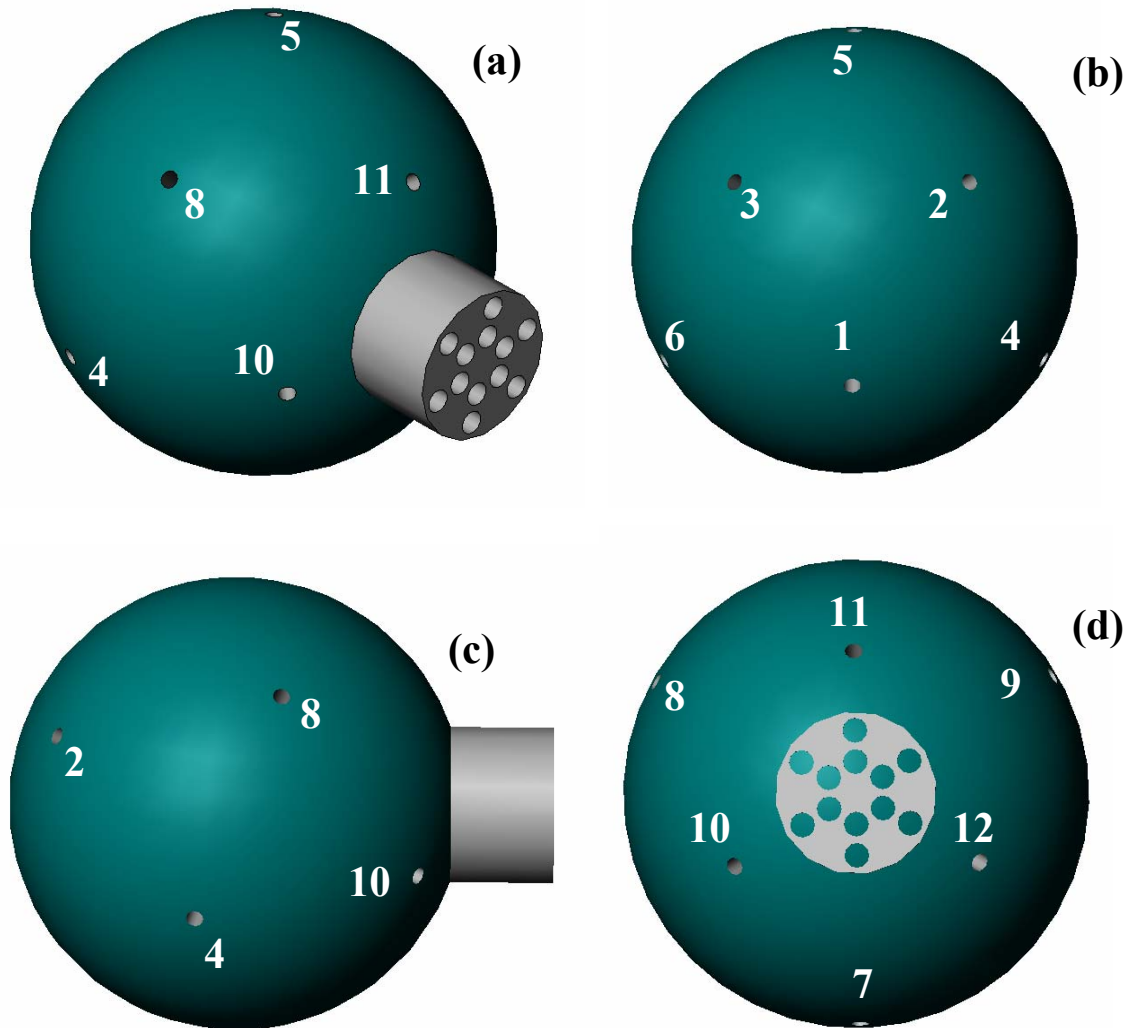
Fig. 23 Model of 12-hole probe for the three-port sting configuration. (a) perspective view, (b) front view, (c) side view, (d) back view. Probe tip diameter: 3/8", ratio of sting diameter over probe diameter: = 0.347, tip hole diameter: 0.014", sting hole diameter: 0.020".

Table 5. Tip port coordinates for two-port sting configuration.

Port Number	Θ (deg)	Φ (deg)
1	31.7175	0.0
2	58.2825	90.0
3	31.7175	180.0
4	58.2825	270.0
5	90.0	31.7175
6	90.0	148.2825
7	90.0	211.7175
8	90.0	328.2825
9	148.2825	0.0
10	121.7175	90.0
11	148.2825	180.0
12	121.7175	270.0

Table 6. Tip port coordinates for three-port sting configuration.

Port Number	Θ (deg)	Φ (deg)
1	37.377	0.0
2	37.377	120.0
3	37.377	240.0
4	79.188	60.0
5	79.188	180.0
6	79.188	300.0
7	100.812	0.0
8	100.812	120.0
9	100.812	240.0
10	142.623	60.0
11	142.623	180.0
12	142.623	300.0

As it was previously mentioned, each one of the sting holes communicates with one of the tip holes/ports. The arrangement of the sting holes is very important because it ultimately dictates the minimum possible sting diameter, which, in turn, affects the maximum possible measurable flow angularity by the probe. The design here was based on a 3/8" tip diameter, a 0.014" tip hole diameter and a 0.020" sting hole diameter. The selection of the tip hole diameter was based on our experience with the 18-hole probe in terms of the minimum possible tip hole diameter that will not suffer from port clogging problems and will yield a reasonable measurement frequency response. Once 0.014" was selected as the tip hole diameter, this automatically dictated a minimum of 0.020" sting hole diameter, based on the availability of stainless steel tubing in the market. As previously discussed, each hole in the sting base mates with a metal tube which ultimately connects each of the tip ports to a corresponding pressure sensor. The minimum-wall-thickness, 0.014"-I.D. stainless steel tube available in the market has an O.D. of 0.020", hence the selection of the sting hole diameter. The geometric values chosen above and the fact that, for fabrication reasons, there has to be a distance of at least 0.005" between the edges of adjacent sting holes, dictate the optimal sting hole configuration (optimal in terms of minimizing sting diameter) shown in Fig. 22d. For the 2-port sting configuration, the minimum possible ratio sting diameter over tip diameter is 0.324. If this is compared to the corresponding ratio for the 18-hole probe (0.347), the reader can see that the sting is significantly smaller for the 12-hole probe case, resulting in reduced sting interference and increased measurable flow angularity.

For the three-port sting configuration, Fig. 23 presents a perspective view of the tip (Fig. 23a), and front, side and back views of the tip (Fig. 23b, Fig. 23c, Fig. 23d respectively), illustrating the location and numbering of the ports. In this case all ports are shown. Fig. 23d also illustrates the arrangement of the holes on the base of the sting. For the three-port sting configuration, this sting hole arrangement is optimal (for the same tip, tip hole and sting hole diameters, i.e. 3/8", 0.014" and 0.020", respectively), although, as expected, it is different from the optimal sting hole arrangement of the two-port sting

configuration. The resulting ratio of sting diameter over tip diameter is 0.347. As seen here, the minimum sting diameter, for the three-port sting configuration, is a little bigger than the minimum sting diameter for the two-port sting configuration and the same as the 18-hole. However, the nearest port to the sting is further away (than that in the 18-hole) thus enabling increased measurable flow angularity.

Algorithm Applied to the 12-Hole Probe

Pressure data for the 12-hole probe was theoretically generated using equation (6). The non-dimensional coefficients for a typical sector (#60107) were plotted using TableCurve 3D for inspection. Fig. 24 and Fig. 25 show the C_θ and C_ϕ plots respectively. The surfaces are flat and sensitive only to their respective flow angle coordinates.
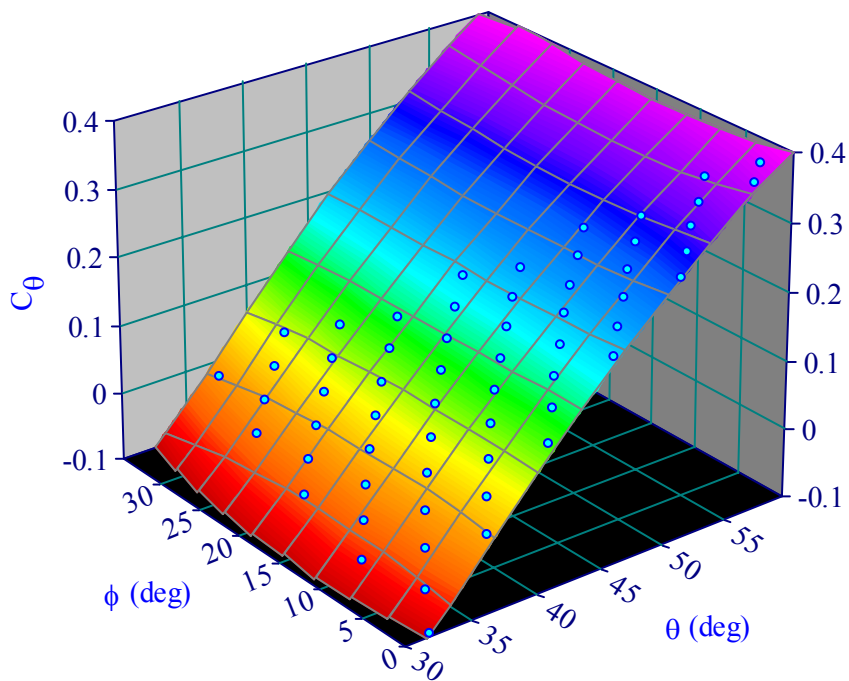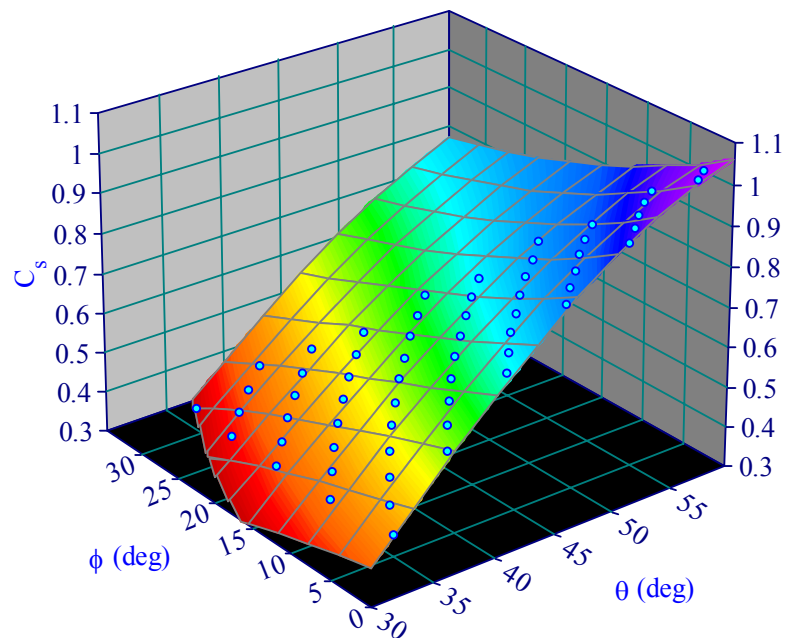

Fig. 24 Typical behavior of the newly-defined cone angle coefficient (equation 21) for a sector of the 12-hole probe (theoretical data).
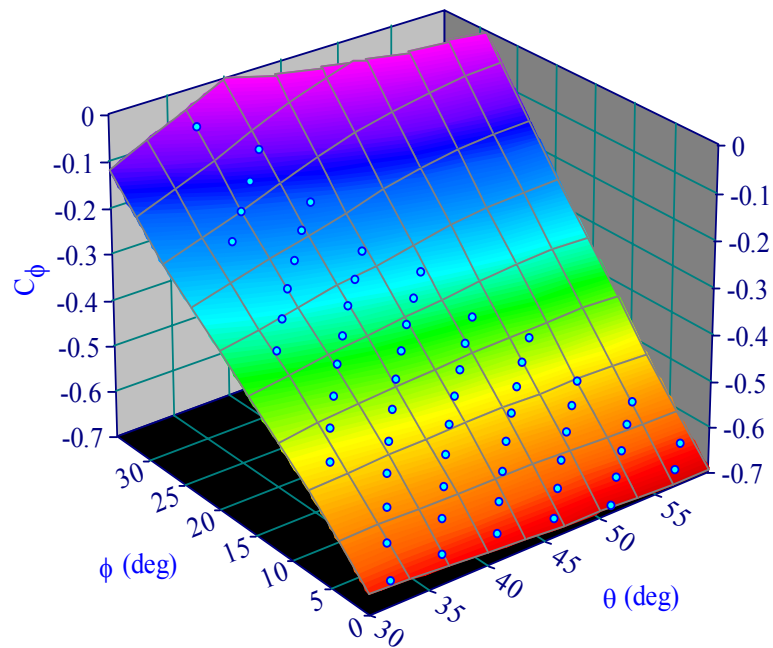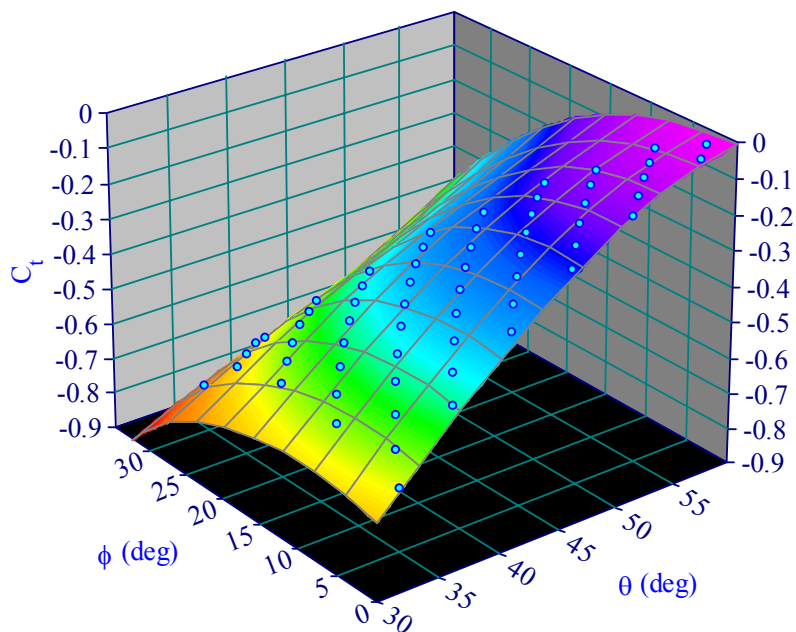
Fig. 25 Typical behavior of the newly-defined roll angle coefficient (equation 22) for a sector of the 12-hole probe (theoretical data).

The Cs and Ct plots are shown in Fig. 26 and Fig. 27. These are well-behaved surfaces with no sharp gradients.

Fig. 26 Typical behavior of the newly-defined static pressure coefficient (equation 23) for a sector of the 12-hole probe.

Fig. 27 Typical behavior of the newly-defined total pressure coefficient (equation 24) for a sector of the 12-hole probe.

Finally the q_{est} plot is also checked in Fig. 28. The surface is nearly constant as desired.
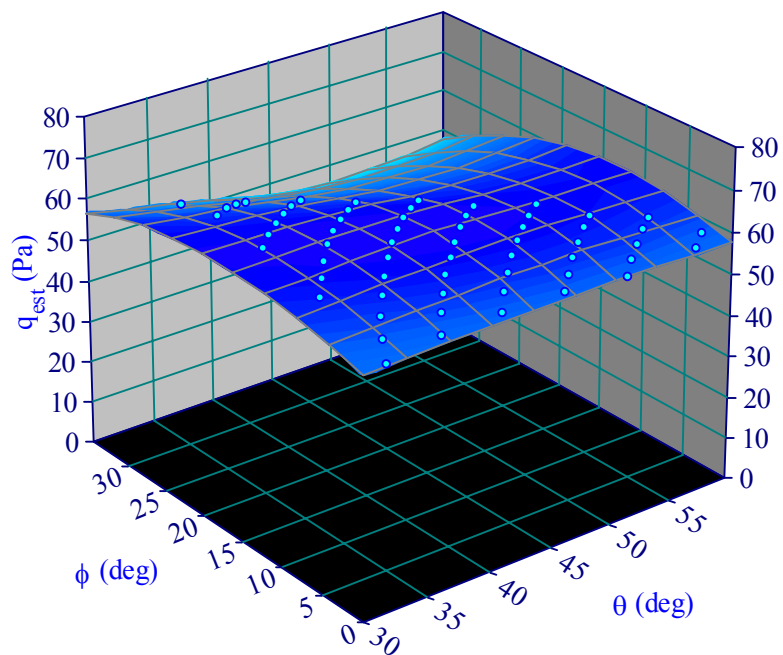
Fig. 28 Typical behavior of the newly-defined estimated dynamic pressure (equation 16) for a sector of the 12-hole probe.

The behavior of the coefficients, as is evident from the plots, suggests very good prediction capability of the reduction algorithm when applied to the 12-hole probe.

The reduction was done with theoretical pressure data generated similar to the 18-hole probe case explored earlier. The statistical error data for the predicted flow quantities is shown in Table 7. In the absence of sting interference effects and experimental inaccuracies not incorporated by the theoretical data, the errors are very small. It signifies that a decent prediction is achievable when the probe is put to test in an actual flow field.

Table 7. Error data for the predicted variables for a 12-hole probe at U=10m/s.

	Maximum	Mean (μ)	Standard Deviation (σ)
Error in Θ (deg)	0.243	0.000	0.028
Error in Φ (deg)	0.232	0.000	0.035
Error% in U	0.148	-0.008	0.030
Error% in P_s w.r.t q	0.210	0.003	0.019
Error% in P_t w.r.t q	0.370	-0.012	0.050

9   SUMMARY AND CONCLUSIONS

The traditionally-used algorithms for the multi-hole probes require a symmetric arrangement of ports, an attribute absent in the 18-hole and the newly-designed 12-hole probes. Novel definitions for the non-dimensional coefficients developed here obviate this necessity. The new algorithm uses only 4 pressure ports at any measurement point thus also avoiding redundancy.

The 18-hole probe has immense application in omni-directional flowfield measurement. An optimized version of the 18-hole probe, the 12-hole probe, was designed, which has the same functionality as the former but with many more advantages. The algorithm developed here is easily applicable to the 12-hole probe also.

High accuracy of prediction of the flow variables was obtained with data from the 18-hole probe – within 0.25 deg in Θ, 0.45 deg in Φ and 0.4% in velocity magnitude, all with 99% confidence. The algorithm is applicable in the entire subsonic regime. Indeed, with the 18-hole probe, the flowfield was resolved up to a Mach number of 0.7 with very small errors.

REFERENCES

[1]   Bryer, D. W., and Pankhurst, R. C., 1971, "Pressure-Probe Methods for Determining Wind Speed and Flow Direction," Her Majesty's Stationary Office, London.

[2]   Everett, K. N., Gerner, A. A., and Durston, D. A., 1983, "Seven-Hole Cone Probes for High Angle Flow Measurements: Theory and Calibration," AIAA J., **21**, No. 7, July, pp. 992-998.

[3]   Kjelgaard, S. O., 1988, "Theoretical Derivation and Calibration Technique of a Hemispherical-Tipped, Five-Hole Probe," NASA Technical Memorandum 4047, Sept.

[4]   Zilliac, G. G., 1989, "Calibration of Seven-Hole Probes for Use in Fluid Flows with Large Angularity," NASA Technical Memorandum 102200, Dec.

[5]   Rediniotis, O. K., Hoang, N. T., and Telionis, D. P., 1993, "The Seven-Hole Probe: Its Calibration and Use," in *Forum on Instructional Fluid Dynamics Experiments*, **152**, June, pp. 21-26.

[6]   Kinser, R. E., and Rediniotis, O. K., 1998, "Development of a Nearly Omnidirectional Velocity Measurement Pressure Probe," AIAA J., **36**, No. 10, pp. 1854-1860.

[7]   Gettelman, C. C., and Krause L. N., 1951, "Characteristics of a Wedge with Various Holder Configurations for Static-Pressure Measurements in Subsonic Gas Streams", NACA Research Memorandum E51G09, Sept.

[8]   Centolanzi, F. J., 1957, "Characteristics of a 40º Cone for Measuring Mach Number, Total Pressure, and Flow Angles at Supersonic Speeds," NACA Technical Note 3967, May.

[9]   Gerner, A. A., and Maurer, C. L., 1981, "Calibration of Seven-Hole Probes Suitable for High Angles in Subsonic Compressible Flows," United States Air Force Academy-TR-81-4.

[10]   Gerner, A. A., and Sisson, G., 1981, "Seven-Hole Probe Data Acquisition System," United States Air Force Academy-TN-81-8, Nov.

[11]   Everett, K. N., Gerner, A. A., and Durston, D. A., 1982, "Theory and Calibration of Non-Nulling Seven-Hole Cone Probes for Use in Complex Flow Measurement," AIAA Paper 82-0232, *AIAA 20th Aerospace Sciences Meeting*, Orlando, Jan.

[12]   Ostowari, C., and Wentz, W. H., 1983, "Modified Calibration Technique of a Five-Hole Probe for High Flow Angles," Experiments in Fluids, **1**, pp. 166-168.

[13]   Houtman, E. M., and Bannink, W. J., 1989, "Calibration and Measuring Procedure of a Five-Hole Hemispherical Head Probe in Compressible Flow," Report LR-585, Apr, Delft University of Technology.

[14]   Zilliac, G. G., 1993, "Modelling, Calibration, and Error Analysis of Seven-Hole Pressure Probes," Experiments in Fluids, **14**, No. 1/2, pp. 104-120.

[15]   Johansen, E. S., Rediniotis, O. K., and Jones, G., 2001, "The Compressible Calibration of Miniature Multi-Hole Probes," ASME J. of Fluids Engineering, **123**, pp. 128-138.

[16]   Rediniotis, O. K., and Vijayagopal, R., 1999, "Miniature Multihole Pressure Probes and Their Neural-Network-Based Calibration," AIAA J., **37**, No. 6, pp. 666-674.

[17]   Clark, E. L., Henfling, J. F., and Aeschliman, D. P., 1992, "Calibration of Hemispherical-Head Flow Angularity Probes," AIAA Paper 92-4005, *AIAA 17th Aerospace Ground Testing Conference*, Nashville, July.

[18]   Takahashi, T. T., 1997, "Measurement of Air Flow Characteristics Using Seven-Hole Cone Probes," NASA Technical Memorandum 112194, May.

[19]   Shepherd, I. C., 1981, "A Four Hole Pressure Probe for Fluid Flow Measurements in Three Dimensions," ASME J. of Fluids Engineering, **103**, pp. 590-594.

[20]   Rediniotis, O. K. and Pathak, M. M., 1999, "Simple Technique for Frequency-Response Enhancement of Miniature Pressure Probes," AIAA J., **37**, No. 7, pp. 897-899.

[21]   White, F. M., 1991, "Laminar Boundary Layers," In *Viscous Fluid Flow*, 2nd ed., (Editors) McGraw-Hill, New York, pp. 298.

VITA

Vijay Ramakrishnan

Department of Aerospace Engineering

3141 TAMU

College Station, TX 77843-3141

(979) 845-7541

vijay_r@tamu.edu

M. S. Aerospace Engineering, Texas A&M University, May 2004.

B. Tech. Aerospace Engineering, Indian Institute of Technology-Madras, India, July 2001.